Society for
Mathematical
Biology

ORIGINAL ARTICLE

Check for
updates

Parameter Estimation for Evaporation-Driven Tear Film Thinning

Rayanne A. Luke[1] [iD] · **Richard J. Braun[1]** [iD] · **Tobin A. Driscoll[1]** ·
Carolyn G. Begley[2] · **Deborah Awisi-Gyau[2]**

Abstract

Many parameters affect tear film thickness and fluorescent intensity distributions over time; exact values or ranges for some are not well known. We conduct parameter estimation by fitting to fluorescent intensity data recorded from normal subjects' tear films. The fitting is done with thin film fluid dynamics models that are nonlinear partial differential equation models for the thickness, osmolarity and fluorescein concentration of the tear film for circular (spot) or linear (streak) tear film breakup. The corresponding fluorescent intensity is computed from the tear film thickness and fluorescein concentration. The least squares error between computed and experimental fluorescent intensity determines the parameters. The results vary across subjects and trials. The optimal values for variables that cannot be measured in vivo within tear film breakup often fall within accepted experimental ranges for related tear film dynamics; however, some instances suggest that a wider range of parameter values may be acceptable.

Keywords Tear film · Dry eye · Fluorescent imaging · Optimization

1 Introduction

The tear film (TF) serves to protect the ocular surface as well as promote clear vision. The TF comprises three layers: a thin, oily lipid layer that is 20 to 100 nm or more thick (King-Smith et al. 2011; Braun et al. 2015); an aqueous layer consisting mainly of water (Holly 1973) that is a few microns thick; and a half-micron thick mucin layer called the glycocalyx that sits atop the ocular surface (King-Smith et al. 2004). The lipids slow evaporation of water from the TF (Mishima and Maurice 1961; King-Smith

✉ Rayanne A. Luke
  rayanne@udel.edu

1   Department of Mathematical Sciences, University of Delaware, Newark, DE 19716, USA

2   School of Optometry, Indiana University, Bloomington, IN 47405, USA

🙋 Springer

et al. 2010; Dursch et al. 2018) and a healthy glycocalyx halts dewetting of the ocular surface (Gipson 2004). The lacrimal gland supplies the majority of the aqueous layer of the tear film near the temporal canthus (Dartt 2009) and Doane (1981) suggested that during the opening interblink phase the puncta drains the excess near the nasal canthus. Evaporation of water from the tear film into the air affects the fluid volume (Mishima and Maurice 1961; Tomlinson et al. 2009; Kimball et al. 2010). Osmosis supplies water from the ocular epithelia (Braun 2012; Cerretani and Radke 2014; Braun et al. 2015).

Tear film breakup (TBU) or tear film disruption occurs when a dry spot appears on the eye (Norn 1969), and is often evaporation-driven (Lemp et al. 2007; Willcox et al. 2017; King-Smith et al. 2018). Tear film breakup time (TBUT) is the length of time after a blink and before the appearance of the first dry spot (Lemp and Hamill 1973; Norn 1969). A clinical determination of TBUT is based on the observer's decision that a dark spot has formed and represents TBU (Norn 1986) and it is sometimes obtained as an average of clinicians' estimates (Cho et al. 1992). Studying TBU is important to understanding dry eye syndrome (DES), as it has been suggested that TF instability plays an important etiological role in this disease (Lemp et al. 2007; Willcox et al. 2017).

DES affects between 5 and 50% of the population depending on the diagnostic criteria used, and it diminishes both quality of vision and ocular comfort (Nelson et al. 2017). The disease may cause inflammation, blurry vision, and a gritty or dry sensation (Mertzanis et al. 2005; Miljanović et al. 2007). Etiological roles played by TBU in DES include inadequate lubrication of the ocular surface and hyperosmolarity of the TF (Gilbard et al. 1978; Lemp et al. 2007; Willcox et al. 2017). Both theoretical (Peng et al. 2014a; Braun et al. 2015) and experimental (Liu et al. 2009) results suggest that osmolarity is elevated by evaporation in TBU; TF osmolarity is one of the metrics used clinically for testing for DES (Lemp et al. 2011; Wolffsohn et al. 2017). In the first DEWS report, Lemp et al. (2007) defined three classes of dry eye: aqueous tear-deficient dry eye (ADDE), evaporative dry eye (EDE), and a mixture of the two.

The normal tear film has an osmolarity in the range 296–302 mOsM (Lemp et al. 2011; Tomlinson et al. 2006; Versura et al. 2010), while healthy blood ranges from 285–295 mOsM (Tietz 1995). Meniscus osmolarity levels reach 316–360 mOsM in DES (Gilbard et al. 1978; Tomlinson et al. 2006; Sullivan et al. 2010; Dartt and Willcox 2013), causing the cornea to be exposed to high salt levels. Concentrations as high as 900 mOsM were experimentally estimated by Liu et al. (2009). Braun et al. (2015) and Peng et al. (2014a) reproduced similar or higher values in mathematical models of tear film break up (TBU), and Li et al. (2015) did so for models of the whole ocular surface. These estimates provide insight since osmolarity may only be measured in the inferior meniscus in a clinical setting (Lemp et al. 2011). Of interest in this article is the osmolarity of the tear film during thinning up to full-thickness tear breakup (FT-TBU), when there is effectively no aqueous layer between the lipid layer and the glycocalyx. Braun (2012) and Braun et al. (2015) found that when modeling the TF as a spatially uniform film, thinning due to evaporation gave rise to osmolarity values up to ten times the isotonic concentration. The model presented in Braun et al. (2018) for TBU development with tangential flow and spatial variation of the TF found smaller peak omolarity levels due to diffusion and smaller evaporation rates. We find

even smaller peak levels of TF osmolarity in our fits; our results may underestimate the true osmolarity in vivo where some slow thinning may continue past the fit interval.

Imaging of the tear film is an important tool for analyzing its dynamics. Common imaging techniques include fluorescence imaging (King-Smith et al. 2013b), spectral interferometry (King-Smith et al. 2004, 2009) and optical coherence tomography (Wang et al. 2003). Dyes such as fluorescein have been used to assess the ocular surface condition by staining the epithelial cells (Norn 1970; Bron et al. 2015, e.g.), estimate tear drainage rates or turnover times (Webber and Jones 1986), visualize general tear film dynamics (Benedetto et al. 1986; Begley et al. 2013; King-Smith et al. 2013a; Li et al. 2014), estimate tear film first breakup times (Norn 1969), and capture the progression of breakup regions (Liu et al. 2006). In what follows, we refer to the fluorescent quantities (e.g., concentration and intensity) using FL. When the FL concentration is below the critical concentration, it is in the dilute regime; when it is above the critical concentration, it is in the self-quenching regime (Webber and Jones 1986). In the dilute regime, the FL intensity is proportional to TF thickness; in the self-quenching regime, TF thickness is approximately proportional to the square root of FL intensity (Nichols et al. 2012; Braun et al. 2014). Simultaneous imaging via interferometry for the lipid layer thickness and FL intensity for the aqueous layer found TBU is caused by different mechanisms (King-Smith et al. 2013b). One observation of TBU formation was clearly consistent with evaporation through small holes in the lipid layer (King-Smith et al. 2013b). Braun et al. (2015) found that flow inside the tear film during TBU can advect fluorescein and thereby change the expected appearance of the TBU; this can complicate interpretation of FL imaging. Simultaneous FL imaging and retroillumination (RI) are another combination that can help interpret tear film dynamics (Himebaugh et al. 2012).

Models with one independent space dimension have been developed to study TBU. Surface tension, viscosity, gravity and evaporation are often incorporated into 1D models; wetting forces have been included as well. Sharma and Ruckenstein built on previous work to include a mucus layer in their models with van der Waals-driven breakup (Sharma and Ruckenstein 1985, 1986). Zhang and coworkers extended two-layer film theory to include van der Waals forces in both mucus and aqueous layers, as well as surfactant transport (Zhang et al. 2003, 2004). They found that van der Waals forces drove the mucus layer to be unstable and the TF to rupture; both instabilities were interpreted as TBU.

Recent TF thinning models have included osmolarity to better to understand the hyperosmolarity in TBU. Braun (2012); Braun et al. (2015) studied an ordinary differential equation model that included constant evaporation at the tear/air interface and osmotic flow at the tear/cornea interface proportional to the osmolarity increase above the isotonic value. The model predicted an equilibrium TF thickness greater than the thickness of the glycocalyx for sufficiently large permeability of the tear/cornea interface. Braun (2012) included van der Waals forces that stopped thinning at the glycocalyx, which allowed a zero permeability condition to be used at the tear/cornea interface.

These models were extended to include space-dependent evaporation by Peng et al. (2014a). Peng et al. (2014a) developed an evaporation distribution with two parts: a stationary, variable-thickness lipid layer with fixed resistance to diffusion of water, and

a resistance to transport in the air. The air resistance included convective and diffusive transport outside the tear film. Peng et al. (2014a) found that osmolarity levels were elevated in TBU regions driven by evaporation, and that diffusion of solutes out of the TBU region prevented osmosis from stopping thinning. Braun et al. (2015) and Braun et al. (2018) used a Gaussian or hyperbolic tangent evaporation profile with an elevated (central) rate larger than the surrounding constant rate. All of the models found that thinning in the TBU region caused by increased evaporation led to elevated osmolarity levels there, which could be several times the isotonic value. The scaling choices in Braun et al. (2018) allowed them to determine when capillary flow balances or dominates viscous effects, thus allowing evaporation to cause TBU. Diffusion is shown to be of greater importance for the osmolarity distribution than advection; the reverse is true for fluorescein. Braun and coworkers highlighted the effect of the FL concentration regime on FL intensity and understanding TBU dynamics from FL images.

Other mechanisms causing TBU have been proposed and studied. Evaporation causes relatively slow TF thinning (King-Smith et al. 2010) and cannot explain rapid TBU, whereby a dry spot may form in under a second (King-Smith et al. 2018; Yokoi and Georgiev 2013). Zhong et al. (2019) hypothesized that Marangoni-driven tangential flow drives rapid thinning in some cases, while Yokoi and Georgiev (2013, 2019) suggest that dewetting is to blame in some instances of rapid circular thinning. Zhong et al. (2019) derived a model that includes rapid breakup induced by strong tangential flow caused by relatively thick areas of the lipid layer, which they referred to as globs. The authors extended their work from a 2018 paper in which they developed a Marangoni-driven model for spot or streak rapid TBU caused by tangential flow occurring under and away from a glob of lipid that was able to explain experimental observations. The flow was caused by the Marangoni effect due to a reduction in the aqueous/air surface tension caused by the increase in surfactant concentration in the glob. Zhong et al. (2018) found scalings appropriate for the length and timescales for many cases of rapid TBU. Zhong et al. (2019) extended the model to include solute transport in their study of glob-driven rapid TBU near a glob using FL imaging. The thinning is caused by tangential flow and relatively slower evaporation. The authors used their model to match TBUT with clinical experiments. Like Braun et al. (2018), the authors studied the effect of initial FL concentration on the ability of FL intensity to correspond to TF thickness, and concluded that using an initial concentration in the dilute regime near the critical concentration is optimal for rapid TBU. They noted that if TBUT occurs in over 4 s, the cause of thinning is cooperative: tangential flow dominates early on but evaporation becomes the main mechanism later. This cutoff is similar to the cutoff for short TBU time used by Yokoi and Georgiev (2019) and others, but the reasons for the short TBU assigned by different groups is different. The cases studied here correspond to "random break," a relatively long time in the lexicon of Yokoi and Georgiev (2019).

To our knowledge, no study has been conducted to measure or estimate TF thinning rates in TBU regions in vivo. Studies that measured thinning include Hamano et al. (1981), who used an invasive method in an open chamber to determine evaporation rates, and King-Smith and coworkers, using spectral interferometry (Nichols et al. 2005; Kimball et al. 2010; King-Smith et al. 2010). Kimball et al. (2010) demon-

strated that evaporation plays a major role in thinning of the TF, as thinning was lost when participants donned air-tight goggles. Dursch et al. (2018) computed a weighted average of TF evaporation rates over the cornea combined with a heat transfer analysis and thermal imaging. Their approach averaged pure water rates and slow rates from a functioning lipid layer. The Berkeley Flow Evaporimeter measured evaporation over the eye palpebral fissure using controlled conditions (Peng et al. 2014b). Wong et al. (2018) reviewed literature values of measured evaporation rates over the palpebral fissure. All of these studies did not target areas of breakup.

Few TF parameter estimations have been conducted by fitting to experimental data; several papers present related optimization problems, parameter identification schemes, or fitting results. Jossic et al. (2009) wanted to optimize the properties of tear substitutes, and they did this for the capillary number, the fluid shear-thinning index, and a parameter capturing the relative size of surface tension in comparison to shear-thinning. The authors maximized the minimum TF thickness and minimized TF thickness variation so as to promote clear vision; they used literature values and did not fit to in vivo data. They comment on the difficulty of studying the shear-thinning index and relative size parameter independently, an issue we raise in this paper about the ratio of two different parameters. Păun et al. (2018) use MCMC methods to quantify parameter uncertainty and fit a model for pulmonary arterial flow and pressure to data measured from healthy and hypoxic mice over five parameters. One of the five parameters was particularly significant in unhealthy mice. Olufsen and Ottesen (2013) found structured analysis of the correlation matrix to be the best method for identifying parameters of a model for heart rate regulation that could be estimated by fitting to patient data. Their fitting was conducted using the Levenberg–Marquardt algorithm to minimize the least squares error.

In this article, we present the results of our efforts to fit the evaporation-driven TF thinning model developed by Braun et al. (2018) to experimental FL intensity data from normal subjects TFs. These findings include parameter values that have not been determined in vivo for areas of breakup to our knowledge and should be of interest to researchers and clinicians alike. We believe these results will impact the understanding of TF thinning and dry spot formation and serve as a reference point when comparing to dry eye patient data.

This article is organized as follows. We describe the data used and then present the mathematical model for spots; the corresponding streak version is found in the Appendix A.3, along with a derivation of the circular model. Our fitting procedure is then outlined and results are given. Discussion and conclusions follow.

2 FL Images

We use data taken in a study conducted at Indiana University as discussed in Braun et al. (2018); we reiterate a brief description below. The study received approval from the Biomedical Institutional Review Board of Indiana University. Declaration of Helsinki principles were followed during data collection and informed consent was obtained from subjects.
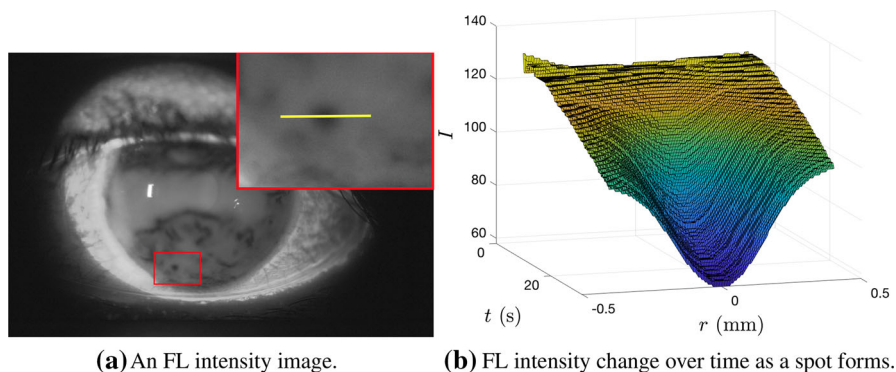
(a) An FL intensity image.   **(b)** FL intensity change over time as a spot forms.

Fig. 1 In **a**, the nasal and temporal sides of the eye are the left and the right, respectively. Inset of **a**: enlargement of box in inferior region. We extract a line of pixel values from across a spot TBU along the line segment shown. This is fit with our theoretical FL intensity function (Color figure online)

The images used are collected using FL imaging. Twenty-five subjects participated in the study. After a screening is conducted, a subject sits for two separate visits with ten trials taken at each visit. Exclusion criteria included (i) contact lens wear and (ii) a DES diagnosis as determined by a clinician. We refer to a trial as the sequence of images of the subject's eye taken every 0.2 or 0.25 s depending on the frame rate. A 2 microliter drop of 2% sodium fluorescein solution is instilled (Carlson et al. 2004). A light with a cobalt blue excitation filter (494 nm wavelength) provides illumination and a Wratten no. 8 barrier filter (yellow) is located in the imaging axis. The aqueous layer of the TF fluoresces green light that is recorded (Lakowicz 2006; 521 nm wavelength). The video recorder starts, and the subject blinks three times to ensure even distribution of fluorescein in the TF. The light level is kept at a predetermined low intensity and an initial FL concentration estimate is calculated using a custom MATLAB code following Wu et al. (2015). We assume the initial FL concentration to be uniform across the cornea. The light source intensity is increased to a predetermined setting after the third full blink, and the subject keeps her eye open as long as possible. The trial concludes when the subject blinks again. The low and high light settings are kept constant across subjects, visits and trials. In what follows, we refer to images in the two light setting regimes as 'dark' or 'bright'. A movie consists of the sequence of images taken during the trial, including the first three blinks at the low light setting and ending after the final blink (Fig. 1).

The following equation gives the fluorescent intensity I (Webber and Jones 1986; Nichols et al. 2012):

$$I = I_0 \frac{1 - \exp(-\epsilon_f h' f')}{1 + (f'/f_{cr})^2} \tag{1}$$

Here, h' is the TF thickness, f' is the FL concentration, ϵ_f is the Napierian extinction coefficient, and I_0 is a normalization factor calculated using model eye measurements.

Asymptotic expansions for fixed h' show that I is approximately linear in the dilute regime but decreases quadratically with increasing f' in the self-quenching regime

(Braun et al. 2014). Instilling the correct amount of fluorescein is important for our purposes; in the dilute regime, TBU may be difficult to identify as the overall images are dark. Our in vivo observations avoid complications that may arise from insufficient contrast or too much saturation by operating in a regime near the peak of the I vs. f' curve (Braun et al. 2018).

During this work, we found a need to distinguish between TBU, as typically understood in the clinic (Norn 1969 and many subsequent papers), and full-thickness TBU (FT-TBU), where the aqueous layer is essentially absent between the lipid layer and the glycocalyx. Sometimes, finding TBU by observing the first dark spot is called fluorescein TBU or FTBU (Yokoi and Georgiev 2013); for the purposes of this paper, we use the term TBU since we only use fluorescein imaging here. Clinically, TBU is typically considered to be the first appearance of a dark spot in the tear film observed directly by the clinician. FT-TBU is computer-aided determination of thinning to a relatively small aqueous thickness. We compare clinical results for TBU and FT-TBU that were blind to the theoretical results below. Our theoretical results correspond more closely to FT-TBU from the clinic.

The rate of decrease of the FL intensity at the center of an area of breakup suggests that the time scale of thinning is important for identifying the mechanism driving TBU formation (Awisi-Gyau et al. 2020). This article focuses on evaporation as the mechanism driving TBU. Tangential flow due to the Marangoni effect is an alternative mechanism that has been modeled as the driving force of rapid TF thinning (Zhong et al. 2019) based on the proposed mechanism of King-Smith et al. (2008). King-Smith et al. (2013b) saw instances of TBU that occurred in a few seconds or less while making observations of dark spot formation by simultaneously imaging the lipid and aqueous TF layers. Zhong et al. (2019) note that evaporation alone cannot produce rapid TBU, citing that it takes at least 8 s to observe a dark spot for a 3.5 μm thick TF with an evaporation rate of 25 μm/min. Thus, evaporation is thought to act on a longer time scale than tangential flow. Kimball et al. (2010) concluded that evaporation is a main mechanism driving decreases in film thickness by using spectral interferometry to observe that TF thinning is often linear in time. This observation suggests that evaporation is often roughly constant in time. In Fig. 2, we compare two TBU instances from the same subject in different trials. The left instance (S27v2t9 1:00) is fit by our evaporation-driven thinning model (see Table 4); the right instance is not. The stark contrast in intensity decrease over time from Fig. 2a, b suggests the possibility of different mechanisms driving TBU, as do the start times of fastest FL intensity decrease: around 4 s (left) versus immediately after the light source intensity is increased to the high setting (right). Furthermore, if the slope of the FL intensity profile starts to level out after some time, it may be that FT-TBU has been reached, or that the TF has thinned to the glycocalyx (Braun et al. 2014) (see Fig. 2).

3 Model

We discuss the model in axisymmetric coordinates; the Cartesian case is described in the Appendix A.3. The TF is modeled as a Newtonian fluid with constant viscosity
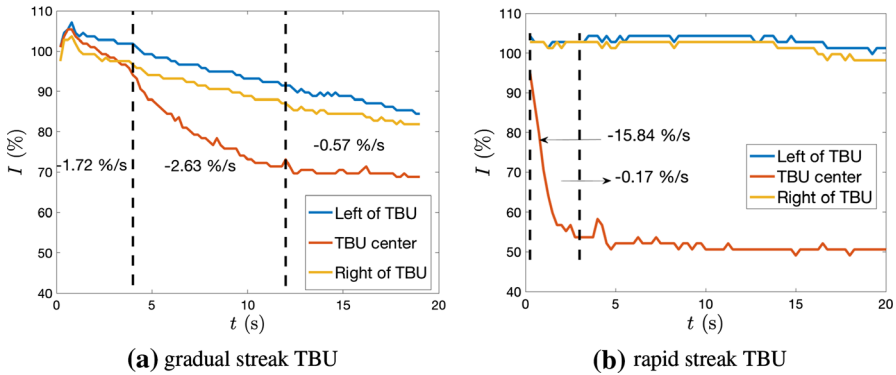
Fig. 2 Comparison of FL intensity change over time of streak TBU from the same subject in different trials, shown with average percentage decrease per second for various time regions during the trial. The data from the left and right of TBU have been taken far enough away from the center of breakup so as to not contain part of the dark streak (Color figure online)

μ and density ρ. The surface tension at the tear/air interface, σ, is assumed constant. The solute diffusivities are assumed constant as well.

3.1 Scalings

The following scalings are used to nondimensionalize the system of equations governing tear film thickness, pressure inside the film, and the transport of solutes in the film. Primes denote dimensional quantities.

$$r' = \ell r, \quad z' = dz, \quad \epsilon = d/\ell, \quad t' = \frac{d}{v_{\max}} t, \quad h' = dh, \quad u' = \frac{v_{\max}}{\epsilon} u,$$

$$v' = v_{\max} v, \tag{2}$$

$$p' - p'_v = \frac{\mu v_{\max}}{\ell \epsilon^3} p, \quad J' = \rho v_{\max} J, \quad c' = c_0 c, \quad f' = f_{\mathrm{cr}} f. \tag{3}$$

The following nondimensional parameters arise from the scalings:

$$S = \frac{\sigma_0 \epsilon^4}{\mu v_{\max}}, \quad A = \frac{A^*}{\mu v_{\max} \ell^2}, \quad P_c = \frac{P_o V_w c_0}{v_{\max}}, \quad \mathrm{Pe}_f = \frac{v_{\max} \ell}{\epsilon D_f}, \quad \mathrm{Pe}_c = \frac{v_{\max} \ell}{\epsilon D_o},$$

$$\phi = \epsilon_f f_{\mathrm{cr}} d'. \tag{4}$$

Dimensional and nondimensional parameters used in the model are summarized in Tables 1 and 2.

3.2 Lubrication Theory

We take a thin film approximation in order to simplify the tear film equations. Appendices A.1, A.2 give details. We assume diffusion, advection, osmosis, and evaporation

Table 1 The dimensional parameters used are shown

Dimensional parameters			
Parameter	Description	Value	Reference
μ	Viscosity	1.3×10^{-3} Pa s	Tiffany (1991)
σ_0	Surface tension	0.045 N m^{-1}	Nagyová and Tiffany (1999)
ρ	Density	10^3 kg m^{-3}	Water
A^*	Hamaker constant	$6\pi \times 3.5 \times 10^{-19}$ s m^{-1}	Ajaev and Homsy (2001)
d	Initial TF thickness	$3-6 \times 10^{-6}$ m	Calculated; see Sect. 2
ℓ	$(\sigma_0/\mu/v_{\max})^{1/4} d$	0.426-0.694 mm	Calculated
$v_{\max}$	Peak thinning rate	0.5-25 μm/min	Nichols et al. (2005)
V_w	Molar volume of water	1.8×10^{-5} m^3 mol^{-1}	Water
h_{eq}	Equilibrium thickness	0.25 μm	Estimated, Gipson (2004)
D_f	Diffusivity of fluorescein	0.39×10^{-9} m^2/s	Casalini et al. (2011)
D_o	Diffusivity of salt	1.6×10^{-9} m^2/s	Riquelme et al. (2007)
c_0	Isotonic osmolarity	300 Osm/m^3	Lemp et al. (2011)
P_o	Permeability of cornea	12.1×10^{-6} m/s	Braun et al. (2015)
ϵ_f	Napierian extinction coefficient	1.75×10^7 m^{-1} M^{-1}	Mota et al. (1991)

The range of estimates for thinning rates are from point measurements from published studies. Some ranges are extended in our results

Table 2 Dimensionless parameters that arise from scaling the dimensional fluid mechanics problem

Nondimensional parameters with typical values		
Parameter	Expression	Value
ϵ	$\dfrac{d}{\ell}$	8.3×10^{-3}
S	$\dfrac{\sigma_0 \epsilon^4}{\mu v_{\max}}$	1
A	$\dfrac{A^*}{\mu v_{\max} \ell^2}$	5.5×10^{-3}
α	$\dfrac{\alpha_0 \mu}{\rho \ell \epsilon^3}$	4.06×10^{-2}
P_c	$\dfrac{P_o V_w c_0}{v_{\max}}$	0.392
Pe_f	$\dfrac{v_{\max} \ell}{\epsilon D_f}$	27.7
Pe_c	$\dfrac{v_{\max} \ell}{\epsilon D_o}$	6.76
ϕ	$\epsilon_f f_{\mathrm{cr}} d$	0.419

The values given are based upon the values of Table 1, $d = 4.5$ μm, and $v_{\max} = 10$ μm/min

contribute to the non-uniform thinning of the TF that ultimately leads to FT-TBU. On the domain $0 < r < R_0$, the system becomes

$$\partial_t h + J - P_c(c - 1) + \frac{1}{r}\partial_r(rh\bar{u}) = 0, \tag{5}$$

$$\bar{u} = -\frac{h^2}{12}\partial_r p, \tag{6}$$

$$p = -\frac{1}{r}\partial_r(r\partial_r h) - Ah^{-3}, \tag{7}$$

$$h(\partial_t c + \bar{u}\partial_r c) = \mathrm{Pe}_c^{-1}\frac{1}{r}\partial_r(rh\partial_r c) + Jc - P_c(c - 1)c, \tag{8}$$

$$h(\partial_t f + \bar{u}\partial_r f) = \mathrm{Pe}_f^{-1}\frac{1}{r}\partial_r(rh\partial_r f) + Jf - P_c(c - 1)f, \tag{9}$$

The spot formation is driven by the evaporative flux J, which we assume comprises a time-independent term and a term proportional to the pressure inside the film. We choose the time-independent term to be Gaussian, so that

$$J(r, t) = v_b + (1 - v_b)e^{-(r/r_w)^2/2} + \alpha p, \tag{10}$$

where v_b is the ratio of the background to the peak thinning rate $v_{\min}/v_{\max}$, r_w is the standard deviation that corresponds to the width of the evaporation distribution, and α is a nondimensional evaporation coefficient. This evaporation coefficient is relatively small, and our results vary only slightly if α is instead set to zero. Thus, we discuss evaporation as if it is time-independent, although in some trials thinning appears to have weak time dependence.

The FL intensity I is computed from the TF thickness h and the FL concentration f:

$$I = I_0\frac{1 - \exp(-\phi f h)}{1 + f^2}. \tag{11}$$

Here, ϕ is the nondimensional Napierian extinction coefficient, and I_0 is a normalization coefficient found using a least squares fit to model eye measurements.

3.3 Boundary and Initial Conditions

We enforce no flux of fluid or solutes at the outer boundary of the domain, $r = R_0$, resulting in homogeneous Neumann conditions for all dependent variables there:

$$\partial_r h(R_0, t) = \partial_r p(R_0, t) = \partial_r c(R_0, t) = \partial_r f(R_0, t) = 0. \tag{12}$$

We assume that a blink restores the TF thickness and solute concentrations to uniform values across the cornea. Thus, the initial conditions are spatially uniform:

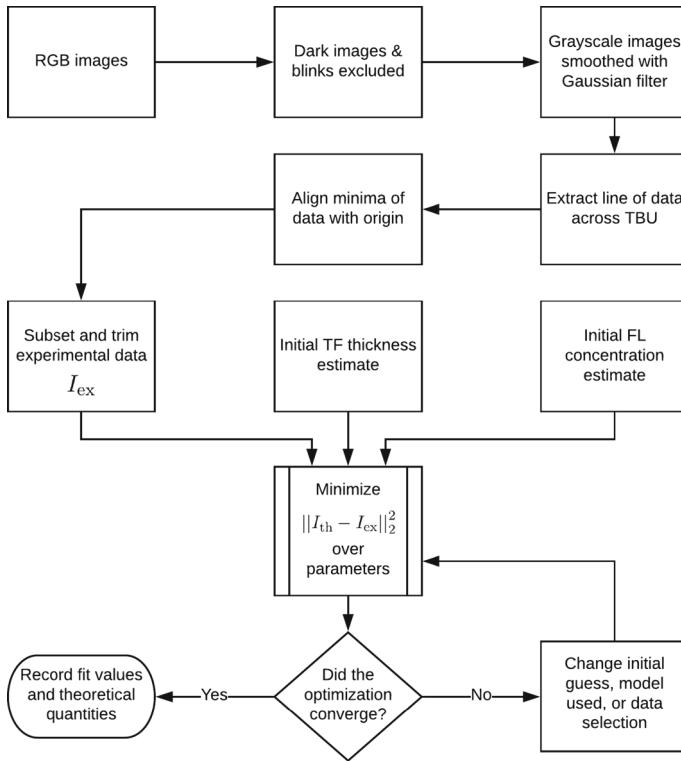$$h(r, 0) = c(r, 0) = 1, \quad f(r, 0) = f_0. \tag{13}$$

Fig. 3 A flowchart of the process by which we prepare the data and conduct the optimization

The initial pressure is computed from (7). The unit initial thickness results from choosing the dimensional initial thickness estimate $h'(r', 0)$ for the characteristic film thickness d'.

3.4 Optimization

We describe the process by which the data is prepared and an optimization is conducted. An overview is given in the flowchart in Fig. 3.

3.4.1 Data Preparation

The images in each trial are converted from RGB color images to grayscale and smoothed with a Gaussian filter. Custom MATLAB codes are used to stabilize the FL intensity images using both the Purkinje (a bright artifact reflecting the light source) and the limbus (the border of the cornea). All dark images and images with partial or complete blinks are excluded. We select a region of interest in the last image where TBU forms (the rectangle in Fig. 1a). For the purposes of this paper, TBU instances are chosen to be a simple shape (roughly linear or circular), dark enough (from monitoring

the local minimum FL intensity), and develop slowly (longer than 4 s). Using a custom MATLAB program, we sample pixel intensities from every bright image in the trial on a line segment across a spot or streak TBU at an orientation that we choose (see inset of Fig. 1a). This data is further stabilized by aligning the minimum of each time level with the origin; the data is shifted by less than 0.1 mm on average. In some cases, asymmetric lighting causes a bias in the intensity where the nasal side is brighter than the temporal side (see Fig. 1a); this is corrected by applying a linear shift to all pixel values to level the intensity at the ends of the sample interval at each time level.

We fit the theoretical FL intensity function to experimental FL intensity data. We use a subset of images from the video, typically selecting every fourth or fifth image; most optimizations use 10–15 time levels from the trial. Any early frames in which no thinning occurs are excluded; the starting frame is the last frame before the FL intensity data starts dropping, as our model assumes thinning starts instantaneously. Similarly, late frames are excluded if the FL intensity data has stopped decreasing or the minimum has begun widening, as our model is not designed to capture this phenomenon. The point in the trial at which the intensity levels overlap each other suggests a minimum thickness of the TF has been reached. Images of all TBU instances fit in this paper are shown in Fig. 18 in Appendix A.4.

3.4.2 Parameter Selection

Many parameters affect the theoretical FL intensity distribution; choosing the ones to optimize over is of crucial importance. Two parameters in particular must be determined separately because they appear only as a combination in the evolution equation for TF thickness. This may be best illustrated by looking at the flat film version of the equations, where spatial derivatives have been neglected. This case is governed by

$$\frac{dh}{dt} + 1 - P_c \left(\frac{h_0}{h} - 1 \right) = 0, \quad h(0) = h_0. \tag{14}$$

Osmolarity c and fluorescein f can be determined by conservation of mass via the relations $hc = h_0$ and $hf = f_0 h_0$. There are two parameters, P_c and h_0; alternatively, we may consider $v_{\max}$ as an implicit parameter and h_0 as an explicit parameter, since $P_c = \frac{V_w P_o c_0}{v_{\max}}$. We note only the combination $\frac{h'_0}{v_{\max}}$ appears in (14). Thus, these two quantities cannot be determined individually via the optimization, but only as a ratio. We may choose to fit P_o, $v_{\max}$, the thinning rate, and h_0, the initial TF thickness. Instead we assume P_o is fixed, but we note that P_o could be found from a fit if we worked with a model that included widening and the stoppage of thinning (Winter et al. 2010).

To estimate an initial thickness estimate, we solve (1) for h'; this gives

$$h' = -\frac{1}{\epsilon_f f'} \log \left(1 - \frac{I}{I_0} \left[1 + (f'/f_{\mathrm{cr}})^2 \right] \right). \tag{15}$$

However, some care is needed to choose f_0', I_0 and I via a separate analysis of the experimental trial as follows. We select a region of the cornea of interest in the last image. In particular, we focus on areas where FT-TBU will form. Across all bright images in the trial we seek the darkest area in the region of interest; the average pixel value from this area is called I_s. The average FL intensity of the center of the region of interest from the first bright image is I_b. We assume the FL concentration has not changed from the last few dark images to the first bright image. The constant I_0 in the FL intensity equation (1) was found using model eye measurements in a low light setting (Wu et al. 2015); we scale I_0 by the ratio of an average of pixel values in the center of the region of interest in the first bright image to that of the last dark image; we replace I_0 with this scaled constant I_0^*. We take $I = I_b - I_s$ as the measured intensity, our scaled I_0^*, and our initial FL concentration estimate $f' = f_0'$ and calculate

$$h_0' = -\frac{1}{\epsilon_f f_0'} \log\left(1 - \frac{I_b - I_s}{I_0^*}\left[1 + (f_0'/f_{\mathrm{cr}})^2\right]\right). \tag{16}$$

Using $d = h_0'$ gives the nondimensional initial thickness value $h_0 = 1$.

We assume that FT-TBU is reached when the TF thickness thins to the thickness of the glycocalyx. This is based on option B for a measurement of the TF thickness given in Fig. 1 of King-Smith et al. (2004); the authors estimate the combined microplicae and glycocalyx thickness to be $1\,\mu\mathrm{m}$. King-Smith et al. (2014) estimate the surface roughness of the epithelium; this suggests a value of $0.5\,\mu\mathrm{m}$ for the epithelial roughness using ± 2 s.d. Govindarajan and Gipson (2010) estimate $0.5\,\mu\mathrm{m}$ as the size of the transmembrane mucins based on earlier reports. Our estimate of $1\,\mu\mathrm{m}$ for the thickness of the glycocalyx is given by adding the values for the roughness and mucin thickness. The mucins that form the glycocalyx serve as a barrier against ions such as fluorescein entering the epithelium from the TF (Govindarajan and Gipson 2010); this suggests that the relevant TF thickness for fluorescent intensity imaging may be measured from the glycocalyx. Thus, from h_0' we subtract an additional $1\,\mu\mathrm{m}$ and use the resulting value as our initial thickness estimate. In this way, zero thickness corresponds not to the cell membrane at the epithelial surface, but to the top of the glycocalyx. This assumption is consistent with the fact that zero intensity is not observed in images of what is thought to be FT-TBU on the cornea. This value is about 20% larger than the cutoff value used by Wong et al. (1996).

We also cannot optimize over the initial FL concentration f_0', since two concentrations, one dilute and the other in the self-quenching regime, correspond to the same FL intensity (see Fig. 4). This estimate is found using a custom MATLAB code as mentioned in Sect. 2.

3.4.3 Optimization Problem

Expressed in continuous variables, we seek to minimize $||I_{\mathrm{th}}(r, t) - I_{\mathrm{ex}}(r, t)||_2^2$ over the parameters $v_{\max}$, the peak evaporation rate, $v_{\min}$, the background evaporation rate, and r_w, the spot evaporation radius. Here, r corresponds to the distance from the center of the spot or streak TBU, and t corresponds to the time after the light source brightness has been increased to the high setting. Both parameters have been nondimensionalized
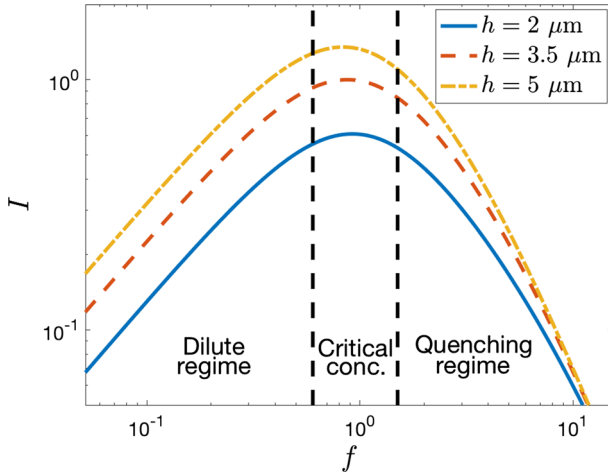
Fig. 4 FL intensity as a function of FL concentration for a fixed TF thickness. The dilute regime is for small f, the critical concentration is near the peak, and the self-quenching regime is for large f (Color figure online)

with the scalings given in Sect. 3.1. The norm is over all $r \in [0, R]$ and $t \in [0, T]$, where R corresponds to the radius of the TBU and T corresponds to the total length of the trial. The nondimensional outer radius, R_0, used to compute I_{th} is chosen large enough to ensure the boundary conditions do not affect the dynamics near the center of TBU; to this end, we widen our computational domain by a factor of about two (in $[0, R_0]$) and compare I_{ex} with the subset of I_{th} corresponding to $[0, R]$. We found that this reduced sensitivity of our optimization to our choices of initial guesses.

The optimization problem may be written

$$\underset{v_{\max}, v_{\min}, r_w}{\text{argmin}} \quad ||I_{\text{th}}(r, t; v_{\max}, v_{\min}, r_w) - I_{\text{ex}}(r, t)||_2^2. \tag{17}$$

The peak evaporation rate $v_{\max}$ corresponds to the TF thickness change in the center of breakup, and the background rate $v_{\min}$ is comparable to a flat film thinning rate computed for an area of the cornea without TBU formation. This uniform thinning rate applies to the model with spatial derivatives ignored [see Eq. (14)].

Some trials exhibit uniform initial thinning before a spot or streak starts to form. We choose to fit these trials with an evaporation function that captures these dynamics:

$$J = v_b + \frac{1}{2} [\tanh(t - t_0 - 2) + 1] (1 - v_b)e^{-(r/r_w)^2/2} + \alpha p, \tag{18}$$

where t_0 is the nondimensional time at which non-uniform thinning begins. This evaporation profile is designed to fully activate non-uniform thinning 4 s after t_0'. In these delayed breakup formation cases, t_0' is added to the optimization as a fourth parameter [see Eq. (18)].

For the purpose of fitting, we define FT-TBUT (full-thickness tear film breakup time) as the time at which the FL intensity stop decreasing. The pixel intensity values typically stop decreasing between 30 and 50 using a 0–255 scale at the illumination settings used.

3.5 Numerical Method and Stopping Criterion

We solve the TF dynamics model (5–9) using an application of the method of lines. The spatial derivatives are discretized using collocation at second-kind Chebyshev points (Trefethen 2000; Canuto et al. 2012). We enforce symmetry at the origin to avoid singularities in the axisymmetric case; this is achieved by expanding all operators in r and dropping odd derivatives. The resulting system of differential algebraic equations for the dependent variables at the grid points is solved using ode15s in MATLAB (MathWorks, Natick, MA, USA). For the optimization, we use a nonlinear least squares minimization implemented by lsqnonlin in MATLAB (MathWorks, Natick, MA, USA) with the Levenberg–Marquardt algorithm (Nocedal and Wright 2006) together with a second-order finite difference approximation of the Jacobian (LeVeque 2007). We verified the method with simulation where optimizations converged as expected with up to 10% added Gaussian noise (unpublished, not shown).

To generate initial guesses for optimization, forward computations were conducted until the theoretical dynamics were close to the experimental. Typically, starting within 20% of the optimal values as an initial guess for the optimization results in parameters that agree with the optimal values to three significant figures. We have found that the Levenberg–Marquardt algorithm works particularly well here, surpassing Nelder–Meade and other options by producing comparatively small residuals while requiring several times fewer iterations (Nocedal and Wright 2006). The comparison with Nelder–Meade was made with data created by forward computations and 10% added Gaussian noise and found that the Levenberg–Marquardt method required over five times fewer iterations (unpublished, not shown). For each instance, the solver stopped because the change in residual was less than the specified tolerance. The default tolerances for both the step size and residual were typically used.

4 Results

We begin by computing sample solutions with a fixed evaporation distribution for a representative spot TBU. Then we proceed to fit initial thickness, evaporation rate and distribution parameters to in vivo fluorescence data. We compare a distribution of our results from fitting to published in vivo local thinning rate measurements via interferometry (Nichols et al. 2005). Finally, we compare clinical and experimental values for TBUT, FT-TBUT, and TBU size.
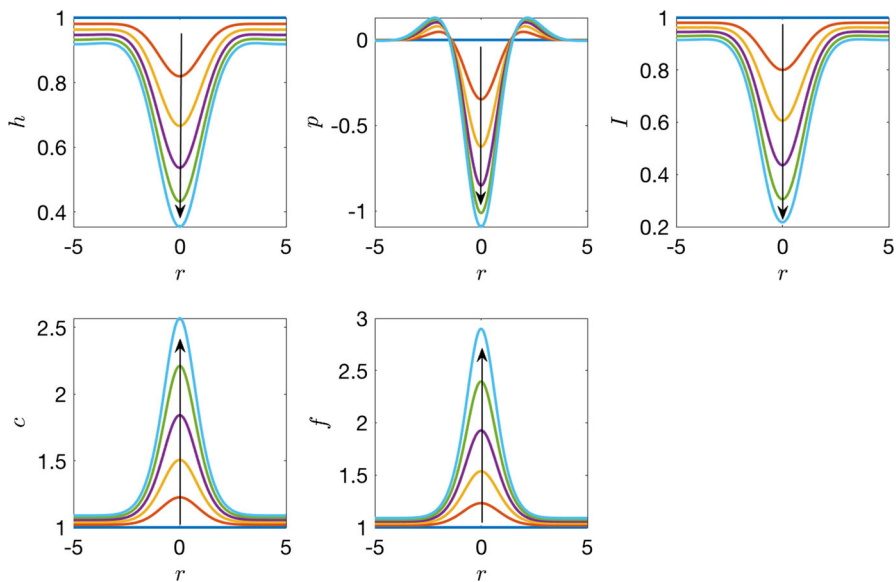
Fig. 5 Nondimensional axisymmetric solutions for $r_w = 0.5\,\text{mm}$, $v_{max} = 10\,\mu\text{m/min}$, $v_{min} = 1\,\mu\text{m/min}$, and $d = 4.5\,\mu\text{m}$. Each curve represents a different time level and arrows indicate increasing time. Intensity has been normalized (Color figure online)

4.1 Nondimensional Solutions

In Fig. 5, we plot the nondimensional axisymmetric solutions for the thickness h, pressure p, osmolarity c, fluorescein concentration f and the fluorescent intensity I. This is a representative solution for a relatively high peak rate of evaporation according to measured results for local thinning in vivo (Nichols et al. 2005), and for what we view as a moderately large spot (Braun et al. 2018; King-Smith et al. 2018). The characteristic length along the film for this case is about 0.5 mm, so the nondimensional spot size is near unity; such spots were viewed as large based on computed FT-TBU times as a function of size (Braun et al. 2018, their Figure 9). The initial thickness and background thinning rates are typical for the computations in this paper. In this and for similar cases throughout this paper, the localized thinning due to evaporation causes elevated solute concentrations and flow inward toward the center of TBU (in all cases, $r = 0$). The decreasing thickness and increasing FL concentration both lower the FL intensity. The intensity thus reflects the thinning of the tear film, though not necessarily in a simple way (Braun et al. 2018; Zhong et al. 2019); the parallels between thickness and FL intensity allow us to infer properties and dynamics of the TF thickness from analyzing FL intensity images. In Fig. 5, we see that regions of positive pressure due to capillarity move fluid in toward $r = 0$, but ultimately fluid is lost to evaporation from the middle of the spot. Here, the film thickness decreases to roughly four tenths of its initial value, while osmolarity increases to over two and a half times its initial amount and FL concentration increases almost threefold. These

results are representative of evaporative FT-TBU; for a more complete exploration in the model, see Braun et al. (2018).

4.2 Fitting

We fit computed FL intensity to in vivo FL intensity measurements. An initial thickness is estimated and fixed, and then the evaporation distribution parameters are adjusted to accomplish the fit. We include several examples of the resulting theoretical solutions using the optimal parameters found by nonlinear least squares minimization. Each TBU instance is labeled by subject, visit, and trial number, the location of the breakup as a clock reading, and the type of breakup (streak or spot). Images showing the TBU instances can be found in Appendix A.4. The streaks are fit with our linear model and the spots are fit with our axisymmetric model. Both the experimental and theoretical FL intensities are normalized to the average of the first time level before fitting, and the osmolarity is reported as a multiple of the isotonic concentration. The optimized parameters are summarized in Tables 3 and 4.

Table 3 Results from fitting over three parameters

Trial	TBU Loc.	TBU type	h'_0 (μm)	f'_0 (%)	v_{max} ($\frac{\mu m}{min}$)	v_{min} ($\frac{\mu m}{min}$)	r_w, x_w (mm)	Min I_{ex}	Min I_{th}	Min h_{th} (μm)
S1v2t7	4:30	—	3.14	0.23	32.0	−4.91	0.0702	0.201	0.254	1.77
S1v2t8	4:30	—	4.64	0.22	19.6	4.46	0.0611	0.187	0.279	2.45
S1v2t10	6:30	○	3.71	0.23	23.6	1.68	0.114	0.118	0.185	2.02
S1v2t10	7:30	—	4.54	0.23	15.8	4.06	0.167	0.162	0.244	2.20
S1v2t10	5:15	—	3.57	0.23	16.4	3.25	0.0780	0.125	0.236	1.99
S1v2t10	3:30	○	2.66	0.23	14.1	2.71	0.0776	0.0955	0.262	1.39
S8v2t3	8:30	○	4.11	0.2	28.7	1.82	0.157	0.189	0.300	2.28
S27v2t9	7:30	—	3.11	0.24	26.2	3.22	0.0554	0.188	0.246	1.24
S28v1t3	6:00	○	5.60	0.21	12.0	2.72	0.0965	0.0444	0.283	3.29

The subject (S) number, visit (v) number and (t) trial number are listed, and the TBU location is a clock reading taken from the center of the pupil. A — denotes streak TBU, and a ○ is a spot. The initial TF thickness and FL concentration estimates are given. The optimized parameters are the peak evaporative thinning rate v_{max}, the background evaporative thinning rate v_{min}, and the spot radius r_w or streak half-width x_w. The minimum values of both the experimental and theoretical FL intensity and the theoretical thickness are reported

Table 4 Results from fitting over four parameters

Trial	TBU Loc.	TBU type	h'_0 (μm)	f'_0 (%)	v_{max} ($\frac{\mu m}{min}$)	v_{min} ($\frac{\mu m}{min}$)	r_w, x_w (mm)	t'_{on} (s)	Min I_{ex}	Min I_{th}	Min h_{th} (μm)
S1v2t10	4:15	○	3.55	0.23	20.0	3.66	0.150	10.5	0.0897	0.136	1.23
S27v2t9	1:00	—	3.86	0.24	20.3	5.32	0.0901	2.49	0.268	0.268	1.88
S28v1t3	9:30	○	4.82	0.21	16.5	3.13	0.138	4.17	0.210	0.249	2.65

The trial, TBU location and type are as in Table 3. The optimized parameters are the peak evaporative thinning rate v_{max}, the background evaporative thinning rate v_{min}, the spot radius r_w or streak half-width x_w, and the time delay t_{on}. The minimum values of both the experimental and theoretical FL intensity and the theoretical thickness are reported
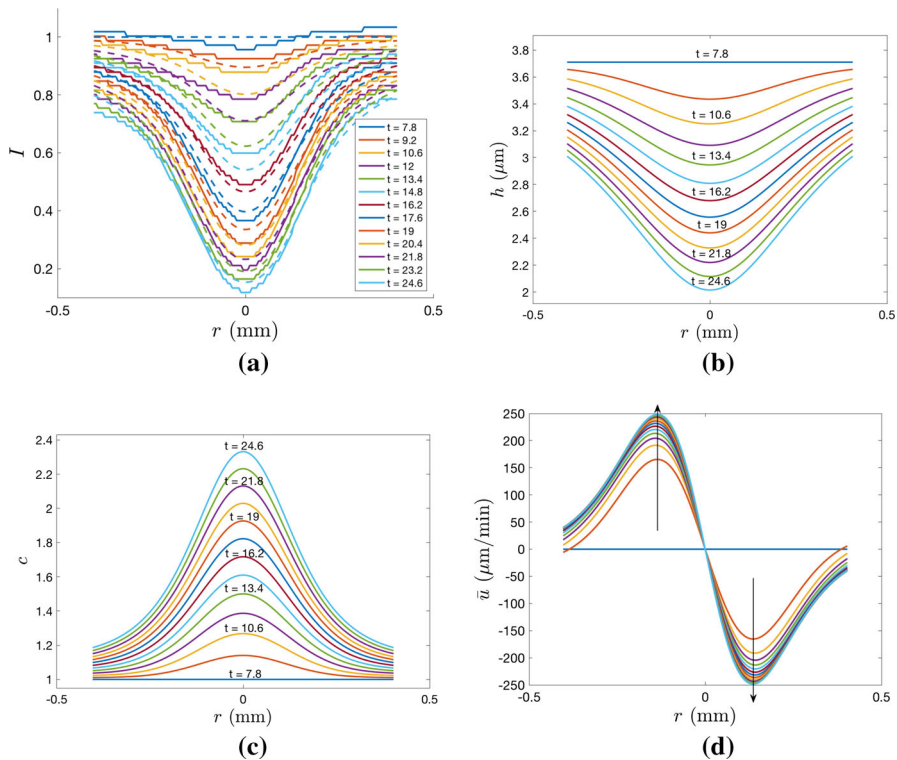
Fig. 6 The S1v2t10 6:30 spot TBU best fit results. **a** Normalized experimental FL intensity (solid lines) with best fit normalized theoretical FL intensity (dashed lines), **b** theoretical TF thickness, **c** theoretical osmolarity as a fraction of the isotonic value, **d** theoretical $\bar{u}$, the depth-averaged fluid velocity, with arrows indicating increasing time (Color figure online)

4.2.1 Spot TBU

We fit the S1v2t10 6:30 spot with the axisymmetric model given in Sect. 3.2; results are shown in Fig. 6. The data from this area of breakup is relatively smooth and symmetric compared to other trials and dry spot regions, which improves the residual when fitting. The FL intensity drops substantially, to less than 20% of its initial value, the TF thickness roughly halves, and the osmolarity roughly doubles. One could expect that a subject would feel irritation and want to blink by the end of this simulation (Liu et al. 2009), though the subject may wait beyond this time interval to blink when instructed to hold the eye open as long as possible.

Although the other dependent variables are even about the origin, the depth-averaged fluid velocity $\bar{u}$ is an odd function with nonzero slope at the center of the spot. Recalling the expression for $\bar{u}$, we expect this quantity to change sign across the center of the spot due to the change in the fluid pressure gradient from negative to positive. We note that the maximum value attained by $\bar{u}$ in each case is much greater in magnitude than the optimal peak thinning rate v_{max}, as expected from our scalings for the velocity components 2.
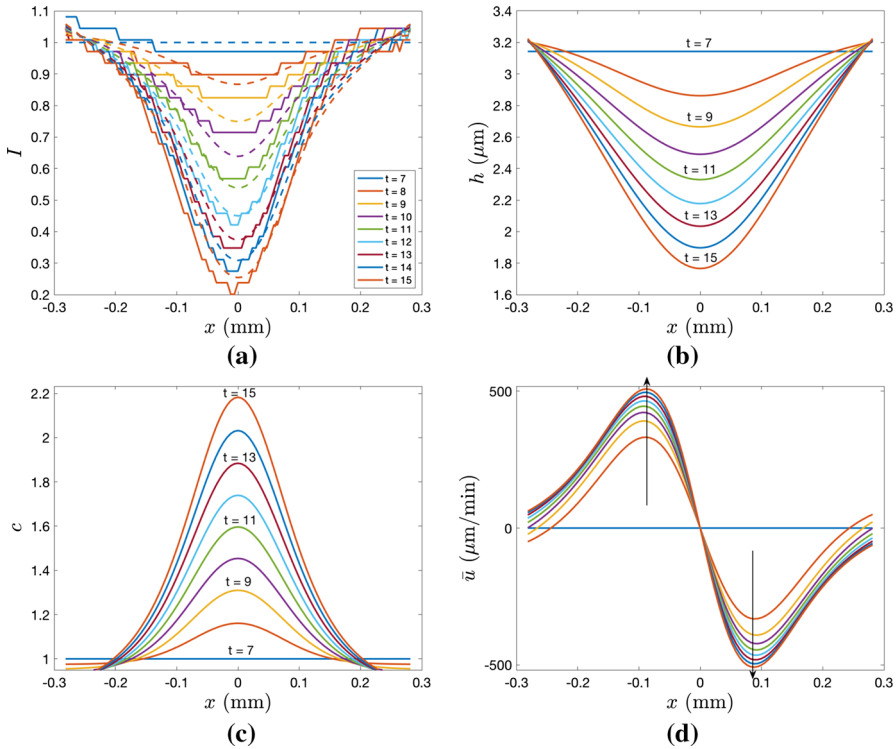
Fig. 7 The S1v2t7 4:30 streak TBU best fit results. **a** Normalized experimental FL intensity (solid lines) with best fit normalized theoretical FL intensity (dashed lines), **b** theoretical TF thickness, **c** theoretical osmolarity as a fraction of the isotonic value, **d** theoretical $\bar{u}$, the depth-averaged fluid velocity, with arrows indicating increasing time (Color figure online)

Calculating the rate of decrease in theoretical TF thickness at the center of the spot gives a thinning rate that is smaller than the optimal v_{max}. This is due to capillary-driven tangential flow into the TBU region. In Fig. 6 we see that the depth-averaged velocity $\bar{u}$ inside the film adds fluid to the TBU region. Osmosis also adds fluid, but more slowly. Evaporation is faster than capillary-driven healing flow and osmosis can oppose it, leading to the TBU seen in Fig. 6.

4.2.2 Streak TBU

We fit the S1v2t7 4:30 streak with the model in Cartesian coordinates (Appendix A.3); results are shown in Fig. 7. The FL intensity drops to about 20% of its initial value, the TF thickness drops to about half of its initial thickness, and the osmolarity more than doubles in center of the streak. The inward flow is about 50% larger than the spot case shown above, with maximum speed around $500\,\mu$m/min.

Results from this fit are summarized in the first row of Table 3; it is the only TBU instance where the optimal v_{min} is less than zero. A negative background thinning rate suggests a thickening of the tear film; this is not expected in TBU. Note that this is

the only TBU instance shown where the theoretical and experimental FL intensity as well as theoretical TF thickness profiles do not exhibit any decrease at the edges of the spatial domain. It is possible that there are other flows occurring in the tear film that are not captured in the model. In the video of the trial, there is a sharp contrast in pixel intensity from non-breakup to the breakup region, which could be an indication of such a flow. The computed fit lags the experimental observations slightly. This lag can also be seen in the previous spot case. It is typical that the theoretical result lags the in vivo FL intensity, but the size of lag can vary. In these first two cases, the decrease in intensity is fairly large, which is good for fitting with evaporation-driven thinning.

4.2.3 TBU with Tilted FL Intensity

We now fit the S27v2t9 7:30 streak with the model in Cartesian coordinates (Appendix A.3). The time levels of the intensity that were fit by the theoretical model are shown in Fig. 8a. The intensity data for this case has been corrected for asymmetric lighting in the preprocessing for fitting. This is seen in the data to varying degrees, as the nasal side of the cornea is brighter on average than the temporal due to light source placement. Although there may be more fluid on one side of the TBU due to flow or lipid layer dynamics causing the asymmetry, for the purpose of fitting with our model we choose use a linear shift in the intensity rather than address these potential physical effects.

In this case, the computed fit lags the experimental observations slightly more than in the previous two cases. The lag tends to be larger in less ideal cases such as this one. The fit is better at later times.

4.2.4 Delayed Non-uniform TBU

We fit the S1v2t10 4:15 spot with the axisymmetric model given in Sect. 3.2; the results are shown in Fig. 9. The time delay is an extension of the model given in Braun et al. (2018). The delay is added due to the lack of information about the lipid layer and about detailed fluid flow in the TF prior to obvious localized thinning. Simultaneous imaging has shown that the TF drifts upward for a short time postblink and that holes in the lipid layer may drift into position some seconds postblink. Subsequent thinning and TBU occurs where the lipid layer holes settle into position (King-Smith et al. 2013b). We speculate that the lipid layer drifts for a time after a blink and brings fluid into the region where TBU later occurs in the trials studied here. Since we base the location of TBU on the last image of the trial (beyond FT-TBU), this may appear in the extracted data as a delay in the formation of a spot or streak.

Once the fit begins, the process is well described by the evaporative thinning model. The intensity again drops about tenfold, the thickness drops to less than half its initial value, and the osmolarity nearly triples. The speed of the tangential flow into the TBU region is relatively small compared to the first two cases. This may be due to the relatively high rate of thinning of the area surrounding the drop; the fit found $v_{min} = 3.5\,\mu m/min$. This would mitigate development of large curvature near the TBU
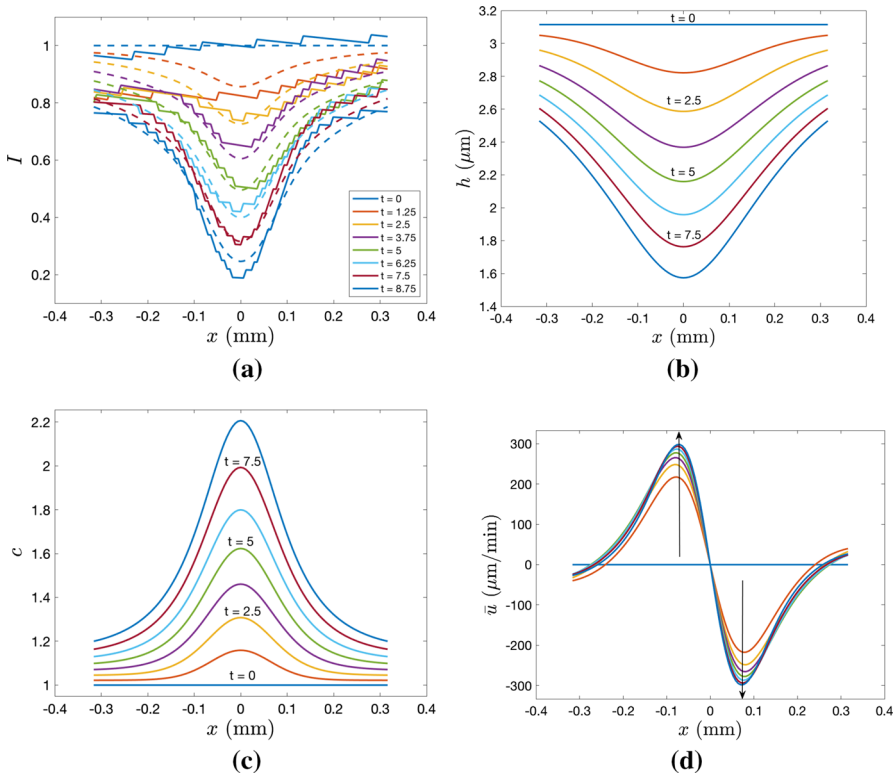
Fig. 8 The S27v2t9 7:30 streak TBU best fit results. **a** Normalized experimental FL intensity (solid lines) with best fit normalized theoretical FL intensity (dashed lines), **b** theoretical TF thickness, **c** theoretical osmolarity as a fraction of the isotonic value, **d** theoretical $\bar{u}$, the depth-averaged fluid velocity, with arrows indicating increasing time (Color figure online)

region and thus decrease the pressure gradient due to capillarity, leading to smaller tangential flow inside the TF.

4.2.5 Simplified ODE Model

We can separate the effect of flow from evaporation and osmosis by considering a simpler model of thinning and TBU. By neglecting spatial derivatives, an ordinary differential equation (ODE) model can be derived for a similar optimization for comparison (see Eq. 14, Braun et al. 2014). We consider two versions: one where evaporation and osmosis are active, and a further simplified model where osmosis is ignored. FL intensity data is extracted from the center of a spot or streak over every bright image in the trial and is fit with both models over a single parameter: a constant thinning rate capturing evaporation.

Figure 10 shows several examples of the best fits given by the two ODE models. The results from the center of the TBU instances as well as from the center of the PDE
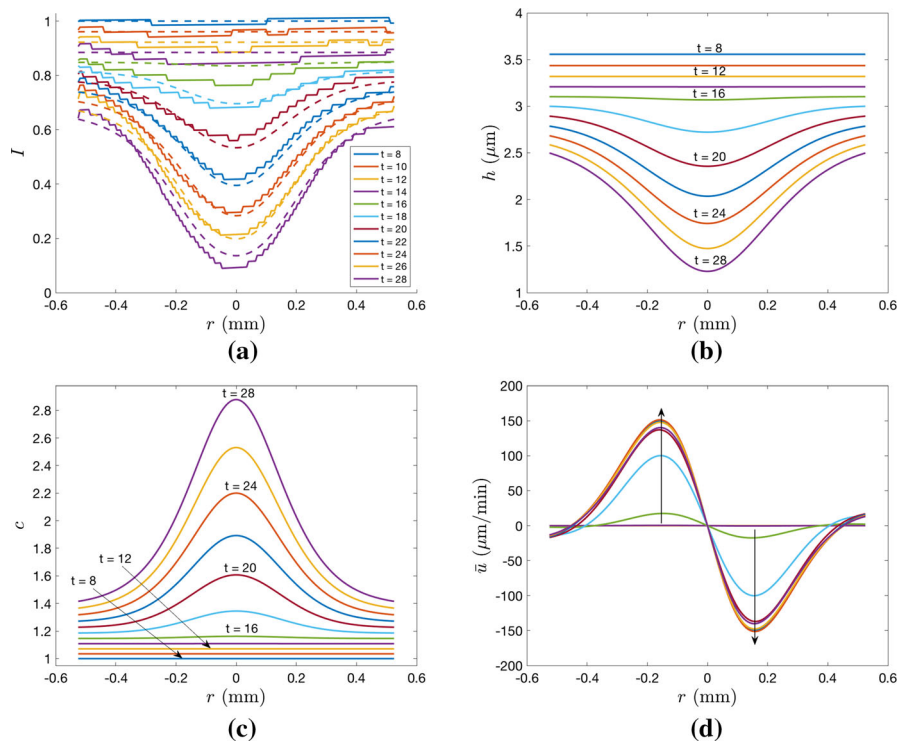
Fig. 9 The S1v2t10 4:15 spot TBU is fit with our axisymmetric model with a time delay. **a** Normalized experimental FL intensity (solid lines) with best fit normalized theoretical FL intensity (dashed lines), **b** theoretical TF thickness, **c** theoretical osmolarity as a fraction of the isotonic value, **d** theoretical $\bar{u}$, the depth-averaged fluid velocity, with arrows indicating increasing time (Color figure online)

model's best fit are also shown. The results from all ODE fitting procedures are given in Table 5.

4.2.6 Aggregate Results

The results of our fitting procedure are given in Tables 3 and 4. The optimal parameter estimates given in Table 4 are similar to those in Table 3 even if one includes the time delay. In this sense, the fits seem robust to small changes in the fitting procedure. However, the approach is far from automatic, and a more sophisticated model that incorporates additional physicochemical effects and types of flow is likely to capture more instances of TBU.

The thinning rates from the ODE fits are on average smaller than those given by the PDE model (see Table 5). We see the ODE models select thinning rates no larger than 18.3 μm/min; the PDE model fits find optimal rates between 12 and 32 μm/min. In some cases, the fit is improved with flow in the model. In other cases, the fits given by the ODE models are superior, suggesting that flow may not play a crucial role in driving the thinning in those cases.
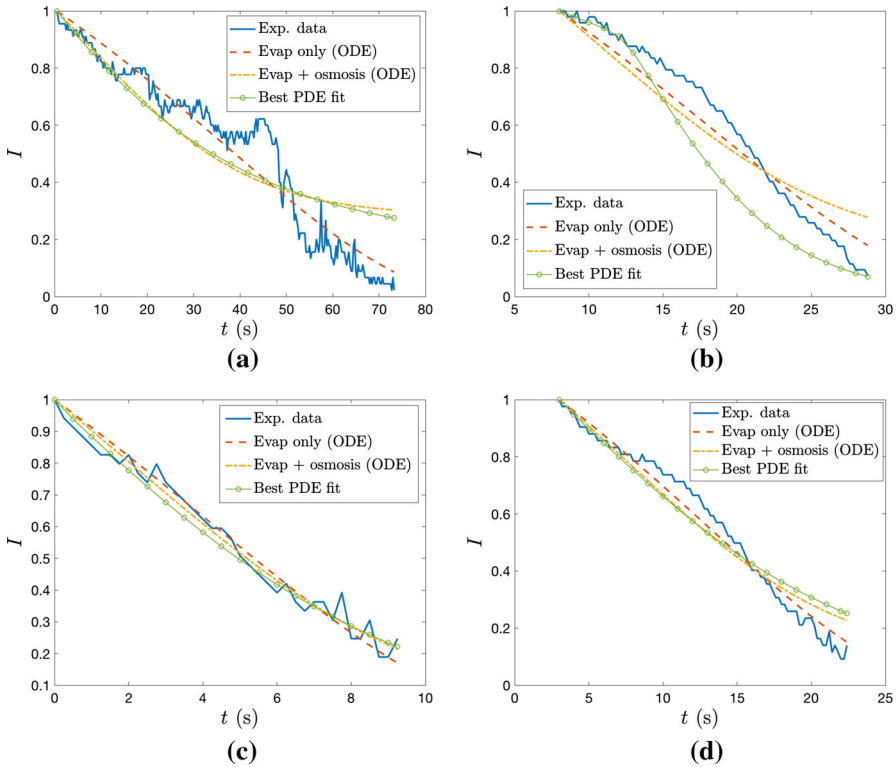
Fig. 10 Several TBU centers are fit with both versions of the ODE model and the center of the PDE fit is included for comparison. Normalized experimental intensity is plotted against normalized theoretical intensity as a function of time. **a** S28v1t3 6:00 spot, **b** S1v2t10 4:15 spot, **c** S27v2t9 7:30 streak, **d** S1v2t8 4:30 streak (Color figure online)

Osmolarity may continually increase during a simulation of the ODE models because diffusion out of the TBU region cannot occur, and so osmosis may increase enough to stop thinning. However, in the PDE case where the film is not flat, diffusion of osmolarity prevents it from becoming large enough to stop thinning (Peng et al. 2014a). If TBU takes long enough, deformation of the TF/air interface spreads well beyond the TBU region, and the computational domain may need to be widened to capture all dynamics and remain consistent with our assumptions.

In Fig. 12, we show aggregate evaporative thinning rates from the optimizations. The histograms have a bin size of $2\,\mu$m/min. Six different trials and four different subjects are represented. For each instance of thinning, we also plot an average of $\partial h/\partial t$ in the center of TBU as given in Eq. 5 for spots and Eq. 45 for streaks. We choose to average from 4 s to the end of the trial to avoid the early phase that is not often fit by experimentalists. Figure 11 illustrates this process and shows that $\partial h/\partial t$ is large in magnitude at the start of a trial and slows considerably in the first few seconds. We also show results from point measurements in vivo due to Nichols et al. (2005). We negated our evaporative thinning rates in order to compare with their results, so

Table 5 Results from fitting for two ODE fits to the center of the breakup data over time

Trial	TBU Loc.	TBU type	h'_0 (μm)	f'_0 (%)	v (E) ($\frac{\mu m}{min}$)	v (E + O) ($\frac{\mu m}{min}$)	v_{max} ($\frac{\mu m}{min}$)
S1v2t7	4:30	—	3.14	0.23	13.9	16.4	32.0
S1v2t8	4:30	—	4.64	0.22	10.1	11.7	19.6
S1v2t10	6:30	o	3.71	0.23	10.1	12.1	23.6
S1v2t10	7:30	—	4.54	0.23	11.2	12.7	15.8
S1v2t10	5:15	—	3.57	0.23	9.09	11.2	16.4
S1v2t10	3:30	o	2.66	0.23	5.36	7.23	14.1
S1v2t10	4:15	o	3.55	0.23	6.85	8.25	15.0
S8v2t3	8:30	o	4.11	0.2	16.8	18.3	28.7
S27v2t9	7:30	—	3.11	0.24	12.0	14.5	26.2
S27v2t9	1:00	—	3.86	0.24	12.5	13.9	17.6
S28v1t3	6:00	o	5.60	0.21	3.62	5.54	12.0
S28v1t3	9:30	o	4.82	0.21	6.86	9.32	13.6

E is the evaporation only model and E + O is the evaporation and osmosis model. The optimal v_{max} from the PDE fit is given for comparison
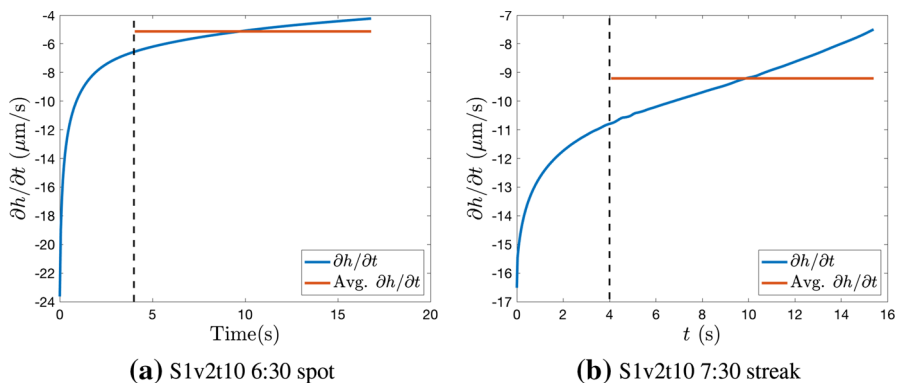

Fig. 11 dh/dt is plotted as a function of time for a spot (**a**) and a streak (**b**). An average is taken starting 4 s into the trial; these values are recorded in Fig. 12 (Color figure online)

that a positive value now indicates thickening of the TF. In their work, Nichols et al. (2005) did not target TBU for their measurements, and so we expect our results to be skewed to larger thinning rates since we only fit areas of TBU. Our range of evaporative thinning rates is similar to that given by the Nichols et al. (2005) distribution, which validates our procedure as one that identifies physically relevant values. We expect the values of $\partial h/\partial t$ to more closely resemble the Nichols et al. (2005) data than our evaporation rates, since that paper recorded thinning rates and not evaporation rates specifically. As may be expected, our overall thinning rates $\partial h/\partial t$ are smaller than the evaporation rates we found. The thinning rate $\partial h/\partial t$ is a combination of three competing mechanisms: evaporation, osmosis, and flow. The first of these serves to thin the film while the second and third thicken the film in the TBU area. Capillarity in
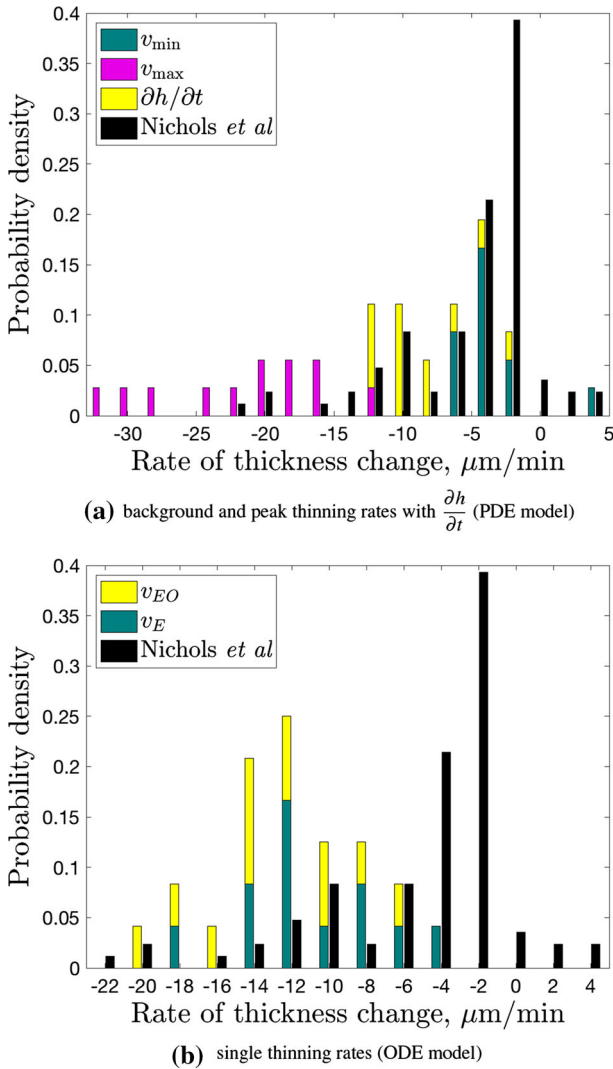
(a) background and peak thinning rates with $\dfrac{\partial h}{\partial t}$ (PDE model)

(b) single thinning rates (ODE model)

Fig. 12 Histograms for pre-corneal TF thinning rates. The peak thinning rates ($v_{\max}$) and background thinning rates ($v_{\min}$) are both are from PDE fits, and the constant thinning rates (v_E, v_{EO}) are from the ODE fits, the first for the model with evaporation only and the second for that with evaporation and osmosis. These are overlaid with point measurements from Nichols et al. (2005) (Color figure online)

particular complicates measurement of the evaporative thinning rate because it drives fresh fluid into the TBU region, reducing $\partial h/\partial t$.

Quantities of interest associated with thinning include the minimum TF thickness attained in an area of breakup and the maximum osmolarity reached in the center of the dry spot. Fig. 13 uses histograms to summarize our results of the minimum thickness and maximum osmolarity from the optimal theoretical solutions. None of our theoretical TF thicknesses approach zero; this may be due to our inability to capture
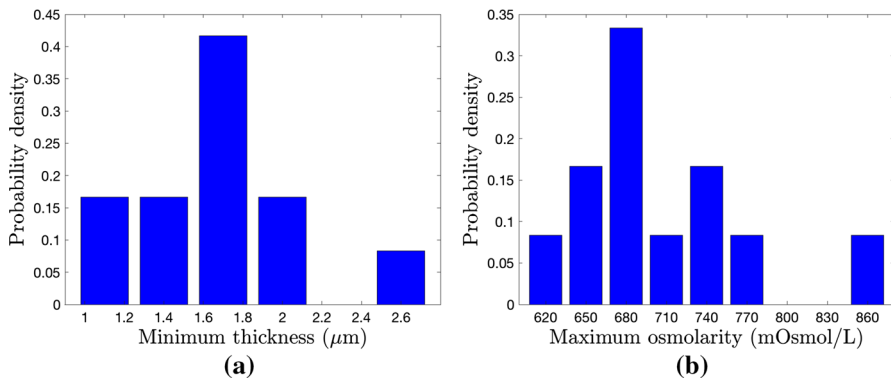
Fig. 13 Histograms from theoretical solutions of all fits of **a** minimum TF thickness and **b** maximum osmolarity (Color figure online)

thinning past FT-TBU, where the thickness may slowly decrease further. In Fig. 13b, we see that maximum osmolarity values cluster around 680 mOsmol/L, or a little over twice the isotonic concentration. The lone outlier to the right is the trial with the longest delayed thinning (the S1v2t10 4:15 spot); the theoretical osmolarity for that instance increases quickly in the middle of the TBU after climbing at a constant rate early on due to the delay (see Fig. 9c).

### 4.2.7 Theoretical and Experimental TBU Time

In Table 6 we present first and last fit times from our optimization, and compare them to clinically determined TBUT and FT-TBUT. Experimental TBU sizes are estimated from thresholding FL images and the optimal widths of our evaporation distribution are also reported there. The last fit time corresponds to what we believe is FT-TBUT, which is the time at which the intensity values in the region of interest (ROI) containing the TBU instance stopped decreasing. The experimental quantity TBUT was determined solely by clinical observation of first dark spot observation and thus does not necessarily involve full thickness tear breakup. FT-TBUT was determined with image processing via a custom MATLAB program (Awisi-Gyau et al. 2020). A clinician thresholded the FL images in the TBU region to observe the breakup and used MATLAB's `regionprops` function to record various quantitative measurements. This data was used to determine experimental sizes of TBU instances at FT-TBUT (Awisi-Gyau et al. 2020). The size (radius) is found by assuming spots are well-approximated by circles. For streaks, we could use MATLAB's `regionprops` to fit the FT-TBU region with either a circumscribing rectangle or an equal-area ellipse. We found that the ellipse fit the FT-TBU region better. The major and minor axes of the bounding ellipse of each TBU instance are found at FT-TBUT. The streak size is taken to be half the minor axis while the spot size is taken to be half the average of the major and minor axes widths. Figure 14 shows an example for the S27v2t9 7:30 streak. Both experimental FT-TBUT times and TBU measurements shown here were determined clinically, without knowledge of our theoretical last fit times or optimal

Table 6 First and last fit times are compared with clinically determined TBUT and with FT-TBUT determined by an optometrist using a custom MATLAB code

Trial	TBU Loc	TBU type	First fit (s)	Last fit (s)	FT-TBUT (s)	TBUT (s)	Est. TBU size (mm)	Opt. r_w, x_w (mm)
S1v2t7	4:30	—	7	15	17.8	10	0.0819	0.0702
S1v2t8	4:30	—	3	21.2	17.8	10.6	0.0421	0.0611
S1v2t10	6:30	○	7.8	24.6	20.2	11.6	0.0498	0.114
S1v2t10	7:30	—	10	25.4	28.6	11.6	0.0963	0.167
S1v2t10	5:15	—	10.8	26.8	30	19.6	0.0498	0.0780
S1v2t10	3:30	○	8	28.8	28.4	18	0.0375	0.0776
S1v2t10	4:15	○	8	28	28.6	16	0.0571	0.15
S8v2t3	8:30	○	2	11	12.75	2.7	0.0798	0.157
S27v2t9	1:00	—	0	8.75	8.25	2.5	0.0912	0.0901
S27v2t9	7:30	—	2	13	23.5	3	0.0572	0.0554
S28v1t3	6:00	○	0.5	70.5	47	8	0.0479	0.0965
S28v1t3	9:30	○	0	27.5	25	6	0.0521	0.138

Estimated TBU size (radius) at FT-TBUT is compared with the optimal width of our Gaussian evaporation distribution

Fig. 14 Illustration of bounding ellipse for the S27v2t9 7:30 streak (contrast enhanced 2×) (Color figure online)
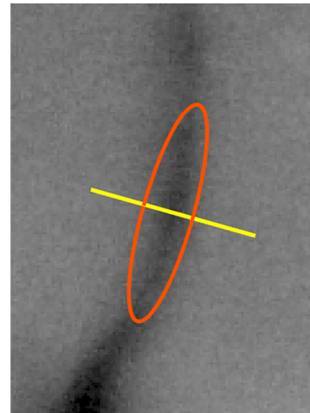
evaporation distribution widths. The radius or width associated with the evaporation of the theory is typically larger than the clinically determined spot size. In all but two cases, the FT-TBUT is within 20% of the last fit time. In contrast, TBUT is about 40–80% shorter than FT-TBUT, and sometimes even less than the last fit time.

In Fig. 15, we overlay data points from our fits with theoretical FT-TBUTs. The FT-TBUTs of our data points have been calculated by using the length of the trial and the time scale $d/v_{\max}$, which depends on the optimal thinning rate. Since we use a glygocalyx thickness of $1\,\mu$m to define TBU, we stop our solver when the film thickness reaches $1\,\mu$m. If we compare Figures 15a, b, we see that small streaks
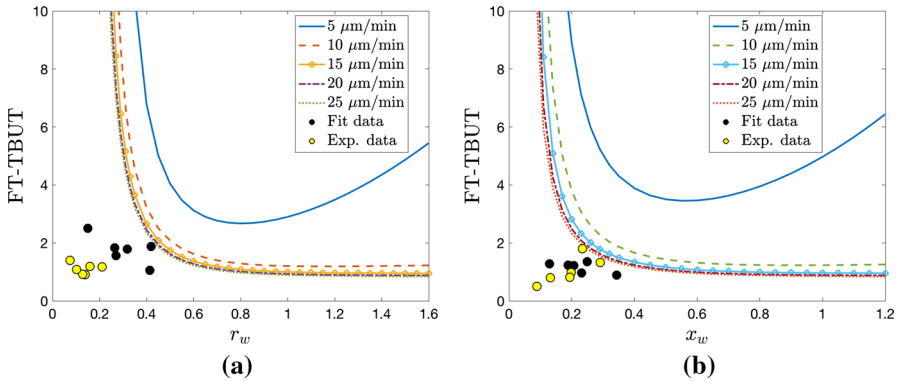
Fig. 15 FT-TBUT as a function of **a** spot width r_w and **b** streak width x_w for $d = 3.5\,\mu$m for five peak thinning rates $v_{\max}$. The spot or streak size is relative to the length scale, ℓ, and FT-TBUT is relative to the time scale. The calculated FT-TBUTs for our fits have been overlaid against their optimal spot or streak widths and experimental FT-TBUTs have been overlaid against their calculated spot or streak widths (Color figure online)

have a shorter breakup time than that of small spots. This may be because spots have curvature in two directions, which drives more flow into the breakup region and slows down thinning.

Our fit data falls below the theoretical curves for FT-TBUT vs r_w or x_w using the $1\,\mu$m cutoff of this paper; there are several reasons as to why this may occur. Many of our TBU spots and streaks are small, and Braun et al. (2018) showed that when r_w is decreased, theoretical FL intensity drops more quickly than TF thickness near the origin due to slow diffusion of fluorescein compared to fast advection (due to capillary action). This makes the spot appear darker, which complicated the optimization. Furthermore, the same 2018 paper showed that a smaller breakup radius increases FT-TBUT, and in particular for spots with nondimensional radius less than 0.25, the FT-TBUT calculated by the model is beyond what is observed in vivo.

The experimental spot data falls below and to the left of the theoretical FT-TBUT curves and our spot fit data. The experimental streak data overlaps with our streak fit data, but still falls below and to the left of the theoretical curves. In general, our optimal spot sizes are significantly larger than the corresponding experimental values. We explore the difference in these values visually for the S1v2t10 4:15 spot in Fig. 16. Qualitatively, the outer circle seems to better capture the entire TBU region. One explanation for the discrepancy is that the threshold used to select the TBU instance to determine the experimental size may be too severe; this would explain the smaller experimental results. Furthermore, the clinical approach finds the minimal circumscribing ROI for the TBU instance without regard to the exact shape of breakup, while we use the resulting data to fit with a predetermined shape of an ellipse or circle. Going forward, we expect the computer-aided clinical and mathematical results to converge. Furthermore, our optimal spot sizes are, on average, larger than our optimal streak sizes. We have mentioned above why circular breakup regions may appear darker than linear ones in FL images; this may cause our optimal spot sizes to be larger than the true TBU radius.
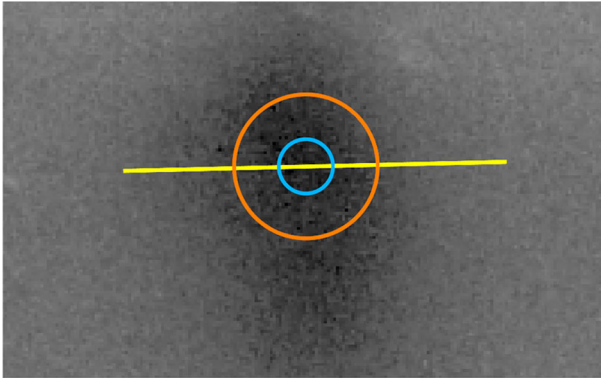
Fig. 16 Illustration of the S28v1t3 9:30 spot with a line of data extracted across it and circles with optimal evaporation distribution radius (outer) and experimental radius (inner) drawn for comparison (contrast enhanced 2×) (Color figure online)

5 Discussion

We fit experimental results by optimizing a small number of parameters that were input into PDE models. Our fits are robust in the sense that they are insensitive to initial guesses and noise, and to small changes in the fitting procedure.

Our models are derived to consider spot or streak formation due to evaporation and tangential flow. However, the fit for the 4:30 streak in trial S1v2t7 (see Fig. 7) appears to have a negative background thinning rate. This would correspond to condensation in the absence of tangential flow. If tangential flow from surrounding tears is directed into the TBU region, then such thickening could occur; however, our models do not take such flows into account. Nichols et al. (2005) recorded point measurements of positive rates of thickness change not necessarily associated with breakup, indicating that this phenonemon does indeed occur. As we focus on fitting instances of TBU instead of arbitrary regions of the center of the cornea, our distribution of rates of TF thickness change, as seen in Fig. 12, is left-skewed in comparison with the Nichols et al. (2005) data. Still, the distributions of point measurements and our optimal values are similar in shape and range, which is indicative of the degree to which our method can accurately capture TF dynamics. Dursch et al. (2018) found a range of 0.6–6 μm/min (here we have used ρ from Table 1 to convert mass flux to thinning rates) but averaged over the cornea with both TBU and intact TF. Peng et al. (2014b) found rates in that range as well with flow evaporimeter experiments. In this work, we emphasized more localized measurements and theory but did not include thermal effects.

During preprocessing of the data, we aligned the minimum thickness in thinning and TBU. The alignment is meant to neutralize the effects of slight eye movement and greatly improves the fitting ability of our optimization. However, drift of the minima over time may be the result of fluid flow that our model does not capture. Although there may be valuable information in quantifying such movement, it is beyond the scope of this paper.

There are two types of delay we observe: The first is a delay in any form of thinning. This may be due to: (i) lipid layer activity preventing thinning that our imaging method cannot capture, or (ii) tangential flow due to upward drift from a blink that prevents local thinning from starting (King-Smith et al. 2013b). It is well known that upward drift due to the Marangoni effect follows the upstroke (Owens and Phillips 2001; King-Smith et al. 2008). There may be other directions of tangential flows depending on location and whether there is ample TF fluid present; in some cases in our trials, tangential flow could be downward from a thick TF or reflex tears (Maki et al. 2008). These tangential flows could cause delay in the onset of TF thinning and breakup when one monitors a fixed location on the cornea. A second type of time delay occurs where the FL intensity remains roughly constant for the first few seconds or more of a trial, and then a localized thinning begins that can drive TBU. There may be several causes for a lag in the start of TF thinning dynamics postblink. We included hypothesized evaporation distributions that mimicked this kind of delay, and this model allowed good fits to such cases.

Another possible source of delay in the start of TBU could be due to it being driven by a dewetting phenomenon (Craster and Matar 2009). It is typical of thinning and dewetting in physical systems that a slow initial period is followed by rapid thinning to rupture, or TBU. This qualitatively fits some cases of TBU formation, and has been proposed by Sharma and others as a mechanism for TBU (Sharma 2003). Dewetting has also been proposed more recently as a mechanism of TBU (Yokoi and Georgiev 2013) for differential DES diagnosis (Yokoi and Georgiev 2019). Future work could quantify whether some signs of dewetting forces are driving TBU in some instances of breakup, perhaps using the methods of Yeh et al. (2013) in which ocular surface regions are located where the glycocalyx has thinned or is defective. If substantially repeatable TBU occurs with significant overlap in the same region of the cornea, then it may be indicative of this phenomenon.

Both the minimum thickness and maximum osmolarity values produced by the model using our initial thickness estimates and optimal parameters are not as extreme as one could expect based on theoretical results (Peng et al. 2014a; Braun et al. 2015, 2018). For all fits that we did, the minimum thickness remains above $1 \, \mu m$, and the maximum osmolarity is around 650 mOsM for most cases (with one exception near 900 mOsM). Figure 13 shows that most cases reached between 600 and 800 mOsM; all of the instances were above the pain threshold in human subjects, about 450 mOsM (Liu et al. 2009). To cause a blink, one may expect TF thickness to go to very small values and for osmolarity to reach three or more times the isotonic level (Liu et al. 2009). The data we fit includes time levels up to FT-TBU but not beyond; there is no spreading of the breakup area or time level curves with repeated minimum intensity value. It is possible that the regime beyond FT-TBU may allow osmolarity to rise to more extreme levels. In summary, the above observations are evidence that elevated osmolarity played a role in subject discomfort, but we cannot say definitively that it lead to the final blink (Varikooty and Simpson 2009; Begley et al. 2013).

Braun et al. (2018) showed that for initial fluorescein values close to half of critical, or 0.1 %, the theoretical TF thickness and FL intensity profiles are quite similar close to and far from the center of breakup (see Fig. 17). In this paper, the initial fluorescein estimates were calculated to be at or above critical concentration. For
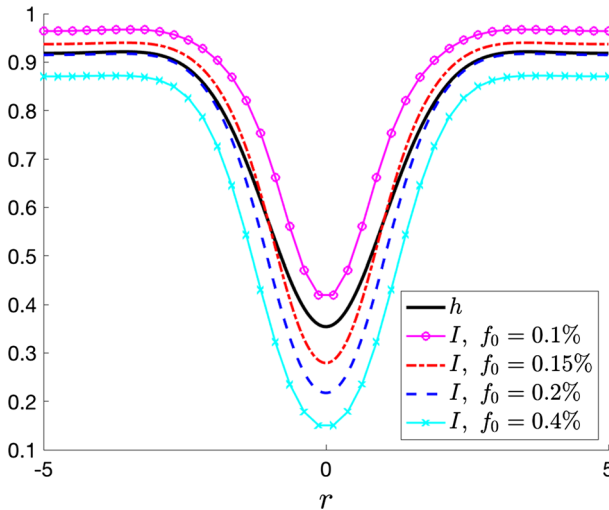
Fig. 17 Normalized theoretical TF thickness h and FL intensity I at $t = 27$ for initial thickness $d = 4.5\,\mu$m, spot width $r_w = 0.5$ mm, peak and background thinning rates $v_{max} = 10\,\mu$m/min and $v_{min} = 1\,\mu$m/min, respectively, for four different initial fluorescein concentrations ($f_0 = 0.2\%$ is the critical concentration). The solid curve is TF thickness and the other curves are FL intensity (Color figure online)

these FL concentrations at 0.2 % or higher, and for small distances from the center of TBU, the theoretical FL intensity gives a relative decrease that is more than that for the TF thickness. This is consistent with our optimal fits, as the theoretical FL intensity decreases more than the theoretical TF thickness. However, as Zhong et al. (2019) suggested for more rapid thinning, a dilute regime may be better for using FL imaging to approximate TF thickness; this may depend on the mechanism driving TBU (King-Smith et al. 2013a).

By fitting with the parameter v_{max}, the peak evaporation rate, we estimate the time scale as the characteristic time until FT-TBU, given by the ratio d'/v_{max}. It is important to note that our model incorporates thinning up to but not beyond FT-TBU. Since we capture thinning up to the point at which the lowest intensities at sequential time levels start to overlap, there may be a minimal further decrease in film thickness that we do not capture. Thus, our fit data may understimate FT-TBUT. This is one of the limitations of the model.

As discussed in the introduction, we expect our results to give higher TF thinning rate values than those found in the literature because we specifically target breakup (Nichols et al. 2005). Hamano et al. (1981) were the first to specifically measure an evaporation rate in humans and obtained a value of $1.45\,\mu$m/min using an invasive method in an open chamber. All using spectral interferometry, Nichols et al. (2005), Kimball et al. (2010), and King-Smith et al. (2010) measured mean thinning rates of $3.79 \pm 4.20\,\mu$m/min (20 subjects), $3.22 \pm 4.27\,\mu$m/min (37 subjects), and $3.4\,\mu$m/min (99 subjects), respectively, with outlier data at or above $20\,\mu$m/min in all three studies. The larger values could correspond to thinning in TBU as suggested by Kimball et al. (2010). Kimball et al. (2010) also reported stoppage of thinning or

even thickening of the TF ($-0.16 \pm 1.78 \, \mu\text{m/min}$) when participants donned air-tight goggles, providing evidence that evaporation plays a major role in thinning the TF. All studies mentioned above did not target areas of breakup; their average values may correspond well to our background thinning rate estimates. The rates above compare well with the estimates of Dursch et al. (2018).

6 Conclusions and Future Work

From our optimizations, we obtain estimates for parameters that cannot currently be measured directly in vivo. The optimal parameter values fall within published ranges of experimental point measurements (Nichols et al. 2005). The in vivo TBU areas tended to be smaller that the theoretical values, perhaps in part due to the assumptions in the theoretical model, and to different experimental protocol in processing images. Slow breakup is best fit by our model, which we assume to be evaporation dominated; an exploration is underway of fits with a Marangoni-driven thinning model for rapid TBU.

Many simplifying assumptions went into our models. One extension may be to formulate the glycocalyx as a porous medium instead of using a no slip condition at the ocular surface; this could promote breakup at shorter times for smaller spots (Nong and Anderson 2010). The TF/air interface was assumed tangentially immobile in this work. Instead, one could assume that an insoluble surfactant plays the role of the lipid layer (Aydemir et al. 2010; Siddique and Braun 2015). Two layer models for the TF system could also be used (see Bruna and Breward 2014; Stapf et al. 2017). Fluorescein imaging is more ambiguous than interferometry and gives no indication of lipid layer dynamics, which may play a crucial role in breakup formation. Including a dynamic lipid layer would alleviate the limited time dependence of our evaporation models. Implementing a fit over two spatial dimensions may work better for this sort of analysis but is not explored here.

We aim to conduct a similar parameter estimation using a model for rapid thinning driven by a glob of lipid creating divergent tangential flow (Zhong et al. 2019). In contrast to this paper, we expect evaporation to play a smaller role in those TBU instances. We expect to identify instances of TBU that are created cooperatively, where thinning is initially lipid-driven but becomes evaporative over time.

The ODE model is a bounding case for the PDE model since it does not include flow, and the corresponding ODE evaporative thinning rates are the smallest we can expect to obtain. Work on adapting the ODE models to allow local fluid flow is underway.

Compliance with ethical standards

Conflict of interest The authors declare that they have no conflict of interest.

A Appendix

A.1 Governing Dimensional Equations

For the circular case, we use the dimensional axisymmetric coordinates (r', z') to denote the position and $\boldsymbol{u}' = (u', w')$ to denote the fluid velocity. The tear film is modeled as an incompressible Newtonian fluid on $0 < r' < R_0$ and $0 < z' < h'(r', t')$, where $h'(r', t')$ denotes the thickness of the film. Conservation of mass and momentum of the TF fluid and transport of solutes within the fluid are given, respectively, by

$$\nabla' \cdot \boldsymbol{u}' = 0, \tag{19}$$

$$\boldsymbol{u}'_{t'} + (\boldsymbol{u}' \cdot \nabla')\boldsymbol{u}' = -\frac{1}{\rho}\nabla' p' + \nu \nabla'^2 \boldsymbol{u}', \tag{20}$$

$$\partial_{t'} s' + \nabla' \cdot (\boldsymbol{u}' s') = D_s \nabla'^2 s', \tag{21}$$

where p' is the fluid pressure and s' represents either c', the osmolarity, or f', the fluorescein concentration, with diffusivities D_o and D_f, respectively. The fluid density is ρ and the kinematic viscosity is ν.

At the film/cornea interface $z' = 0$, we require no slip and osmosis across a perfect semipermeable membrane:

$$u' = 0, \quad w' = P_o V_w (c' - c_0). \tag{22}$$

The membrane permeability is given by P_o, the molar volume of water is V_w, and c_0 is the isotonic osmolarity.

We enforce no flux of solutes across both the film/cornea and film/air interfaces:

$$D_o \boldsymbol{n}' \cdot \nabla' c' - \boldsymbol{n}' \cdot \boldsymbol{u}' c' = 0, \quad D_f \boldsymbol{n}' \cdot \nabla' f' - \boldsymbol{n}' \cdot \boldsymbol{u}' f' = 0. \tag{23}$$

At $z' = 0'$, the outward normal is given by $\boldsymbol{n} = (0, -1)$, and at $z = h'(r', t')$,

$$\boldsymbol{n} = \frac{(-\nabla'_{II} h', 1)}{(1 + |\nabla'_{II} h'|^2)^{1/2}}, \tag{24}$$

where ∇'_{II} is the gradient in the plane of the substrate parallel to $z' = 0$.

The kinematic condition implies that the balance of the material derivative of the TF thickness and the fluid velocity in the $z'-$ direction is controlled by the evaporative mass flux, J':

$$\rho \left[\frac{\partial_{t'} h' + u' \nabla'_{II} h' - w'}{(1 + |\nabla'_{II} h'|^2)^{1/2}} \right] = -J', \tag{25}$$

where

$$J' = \rho \left[v_{\min} + (v_{\max} - v_{\min}) e^{-(r'/r_w)^2/2} \right] + \alpha_0 (p' - p'_v). \tag{26}$$

Here, α_0 is effectively α/K from Ajaev and Homsy (2001), $v_{\min}$ and $v_{\max}$ are background and peak thinning rates, respectively, r_w is the standard deviation that corresponds to the width of the evaporation distribution, and p_v' is atmospheric pressure. The contribution of pressure to evaporation may be ignored with little consequence.

The normal stress condition at $z' = h'(r', t')$ is given by

$$p' - p_v' = -\left(\sigma_0 \nabla_s' \cdot \boldsymbol{n}' + \frac{A^*}{h'^3}\right), \tag{27}$$

where σ_0 is the surface tension, $\nabla_s' = (I - \boldsymbol{n}'\boldsymbol{n}') \cdot \nabla$ (Stone 1990), and A^* is the Hamaker constant.

A.2 Derivation of Tear Film Equations, Spot Case

Using the scalings (2), (3), we nondimensionalize the governing equations as in Braun et al. (2018). At leading order, conservation of mass and momentum of the fluid on $0 < z < h(r, t)$ are given by

$$\frac{1}{r}\partial_r(ru) + \partial_z w = 0, \tag{28}$$

$$\partial_z^2 u = \partial_r p, \quad \partial_z p = 0. \tag{29}$$

The leading order boundary conditions at $z = 0$ are

$$u = 0, \quad w = P_c(c - 1). \tag{30}$$

The leading order boundary conditions at $z = h(r, t)$ are

$$\partial_t h + u\partial_r h - w = -J, \tag{31}$$

$$p = -\frac{1}{r}\partial_r(r\partial_r h) - \frac{A}{h^3}. \tag{32}$$

Integrating (28) over the vertical domain, applying the Leibniz rule, and using (31) and (30) to substitute in for the first three resulting terms gives

$$\partial_t h + J - P_c(c - 1) + \frac{1}{r}\partial_r(rh\bar{u}) = 0, \tag{33}$$

where

$$\bar{u}(r, t) = \frac{1}{h}\int_0^h u(r, z, t)dz \tag{34}$$

is the depth-averaged fluid velocity. The radial velocity u in the tangentially immobile case is given by

$$u(z) = \frac{1}{2}(z^2 - zh)\partial_r p. \tag{35}$$

For solutes, we keep all powers of ϵ before assuming an expansion in this small parameter. The nondimensional solute transport equations are

$$\partial_t s + u\partial_r s + w\partial_z s = \text{Pe}_s^{-1}\left[\frac{1}{r}\partial_r(r\partial_r s) + \epsilon^{-2}\partial_z^2 s\right], \tag{36}$$

where s denotes either osmolarity c or fluorescein concentration f, and $\text{Pe}_s = \dfrac{v_{\text{max}}\ell}{\epsilon D_s}$ is the Péclet number Pe_c or Pe_f, respectively. We continue the derivation for the osmolarity c following Jensen and Grotberg (1993).

The solute boundary condition at $z = 0$ is

$$\epsilon^{-2}\text{Pe}_c^{-1}\partial_z c = wc, \tag{37}$$

and the boundary condition at $z = h(r, t)$ is

$$\partial_z c = \text{Pe}_c\epsilon(u\partial_r h - w)c + \epsilon^2\partial_r h\partial_r c. \tag{38}$$

Assume that $c(r, z, t)$ can be expanded as:

$$c = c_0(r, z, t) + \epsilon^2 c_1(r, z, t) + O(\epsilon^4). \tag{39}$$

After substituting this expression for c into (36), the leading order equation is given by

$$\partial_z^2 c_0 = 0, \tag{40}$$

and thus $c_0 = c_0(r, t)$. The next order in ϵ results in

$$\partial_z^2 c_1 = \text{Pe}_c(\partial_t c_0 + u\partial_r c_0) - \frac{1}{r}\partial_r(r\partial_r c_0). \tag{41}$$

Integrating (41) over the vertical domain gives

$$\partial_z c_1(r, h, t) - \partial_z c_1(r, 0, t) = \text{Pe}_c(h\partial_t c_0 + h\bar{u}\partial_r c_0) - \frac{1}{r}h\partial_r(r\partial_r c_0). \tag{42}$$

The terms involving c_1 can be eliminated by identifying the boundary conditions at $O(\epsilon^2)$; these result in an equation for c_0. We drop the subscript to give our leading

order PDE for osmolarity:

$$h(\partial_t c + \bar{u}\partial_r c) = \frac{1}{r}\mathrm{Pe}_c^{-1}\partial_r(r\partial_r c) + Jc - P_c(c-1)c. \tag{43}$$

The evolution equation for f may be obtained similarly:

$$h(\partial_t f + \bar{u}\partial_r f) = \frac{1}{r}\mathrm{Pe}_f^{-1}\partial_r(r\partial_r f) + Jf - P_c(c-1)f. \tag{44}$$

A.3 Tear Film Equations, Streak Case

The derivation of the problem in the linear case for streaks is similar to the axisymmetric case, and more details may be found in Braun et al. (2015, 2018). The nondimensionalization is the same in both cases.

The problem is solved on $0 < x < X_L$ and $0 < z < h(x,t)$, where h is the TF thickness. Homogeneous Neumann boundary conditions are applied at $x = 0$ and $x = X_L$. The fluid velocity coordinates in the (x, z) directions are given by (u, w). Nondimensionally, the system is given by

$$\partial_t h - J - P_c(c-1) + \partial_x(h\bar{u}) = 0, \tag{45}$$

$$\bar{u} = -\frac{h^2}{12}\partial_x p, \tag{46}$$

$$p = -\partial_x^2 h - Ah^{-3}, \tag{47}$$

$$h(\partial_t c + \bar{u}\partial_x c) = \mathrm{Pe}_c^{-1}\partial_x(h\partial_x c) - P_c(c-1)c + Jc, \tag{48}$$

$$h(\partial_t f + \bar{u}\partial_x f) = \mathrm{Pe}_f^{-1}\partial_x(h\partial_x f) - P_c(c-1)f + Jf. \tag{49}$$

Nondimensionally, the evaporation distribution is given by

$$J(x,t) = v_b + (1-v_b)e^{-(x/x_w)^2/2} + \alpha p. \tag{50}$$

The parameters v_b and α are identical to that in the spot case, and r and r_w have simply been replaced with x and x_w.

A.4 TBU Images

The last image from each trial is shown in Fig. 18 with fitted TBU highlighted. These correspond to the results given in Tables 3 and 4.
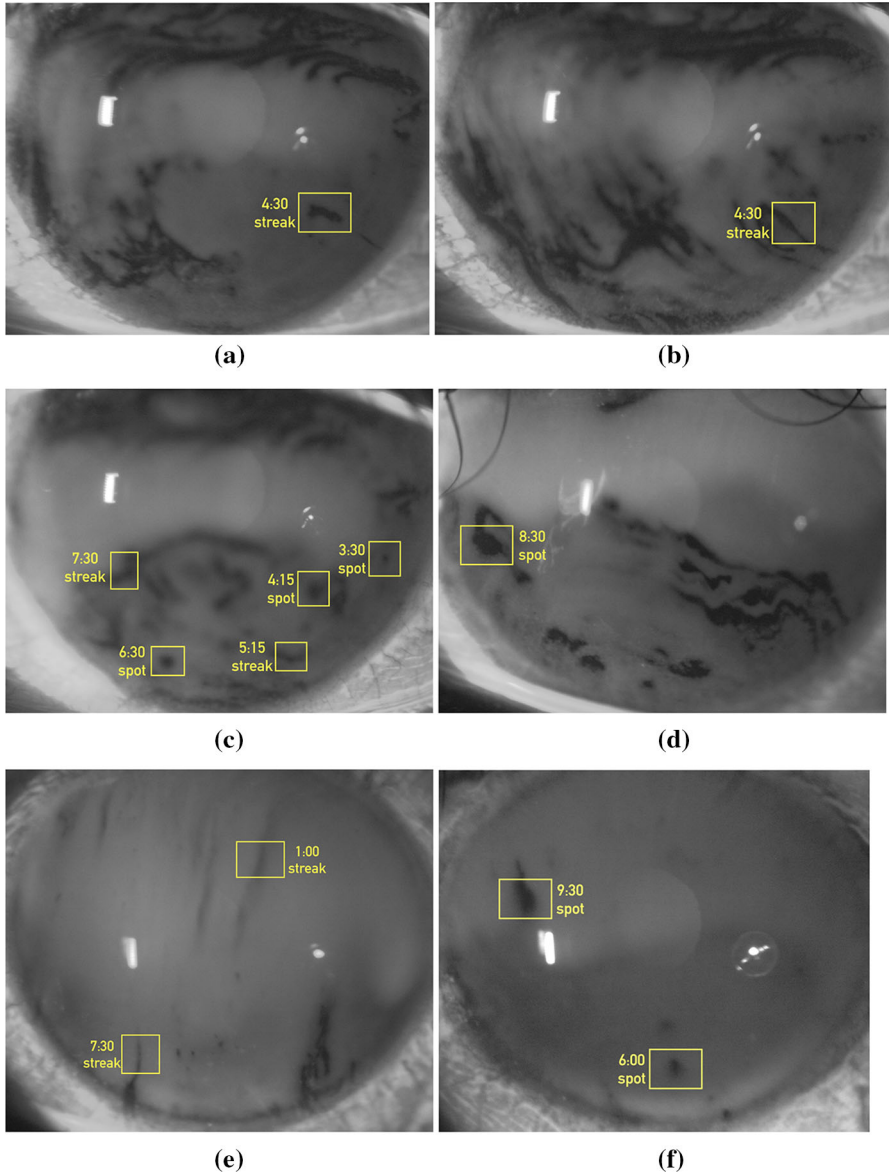
Fig. 18 The last image in each trial: **a** S1v2t7, **b** S1v2t8, **c** S1v2t10, **d** S8v2t3, **e** S27v2t9, **f** S28v1t3 (contrast of **f** enhanced 2×). The bright rectangle, called the Purkinje, is due to the reflection from the light source (Color figure online)

References

Ajaev VS, Homsy GM (2001) Steady vapor bubbles in rectangular microchannels. J Colloid Interface Sci 240(1):259–271

Awisi-Gyau D, Begley CG, Braun RJ, Luke RA, Tichenor A, King-Smith P (2020) Characterization of spatial and temporal properties of tear breakup patterns **(in preparation)**

Aydemir E, Breward CJW, Witelski TP (2010) The effect of polar lipids on tear film dynamics. Bull Math Biol 73:1171–1201

Begley CG, Simpson T, Liu H, Salvo E, Wu Z, Bradley A, Situ P (2013) Quantative analysis of tear film fluorescence and discomfort during tear film instability and thinning. Invest Ophthalmol Vis Sci 54:2645–2653

Benedetto DA, Clinch TE, Laibson PR (1986) In vivo observations of tear dynamics using fluorophotometry. Arch Ophthalmol 102:410–412

Braun RJ (2012) Dynamics of the tear film. Annu Rev Fluid Mech 44:267–297

Braun RJ, Gewecke NR, Begley CG, King-Smith PE, Siddique JI (2014) A model for tear film thinning with osmolarity and fluorescein. Invest Ophthalmol Vis Sci 55(2):1133–1142

Braun RJ, King-Smith PE, Begley CG, Li L, Gewecke NR (2015) Dynamics and function of the tear film in relation to the blink cycle. Prog Retin Eye Res 45:132–164

Braun RJ, Driscoll TA, Begley CG, King-Smith PE, Siddique JI (2018) On tear film breakup (tbu): dynamics and imaging. Math Med Biol 35(2):145–180

Bron A, Argüeso P, Irkec M, Bright F (2015) Clinical staining of the ocular surface: mechanisms and interpretations. Prog Ret Eye Res 44:36–61

Bruna M, Breward CJW (2014) The influence of nonpolar lipids on tear film dynamics. J Fluid Mech 746:565–605

Canuto C, Hussaini MY, Quarteroni A, Thomas A Jr et al (2012) Spectral methods in fluid dynamics. Springer, Berlin

Carlson NB, Kurtz D, Hines C (2004) Clinical procedures for ocular examination, vol 3. McGraw-Hill, New York

Casalini T, Salvalaglio M, Perale G, Masi M, Cavallotti C (2011) Diffusion and aggregation of sodium fluorescein in aqueous solutions. J Phys Chem B 115(44):12896–12904

Cerretani CF, Radke C (2014) Tear dynamics in healthy and dry eyes. Curr Eye Res 39(6):580–595

Cho P, Brown B, Chan I, Conway R, Yap M (1992) Reliability of the tear break-up time technique of assessing tear stability and the locations of the tear break-up in Hong Kong Chinese. Optom Vis Sci 69(11):879–885

Craster RV, Matar OK (2009) Dynamics and stability of thin liquid films. Rev Mod Phys 81(3):1131

Dartt D (2009) Neural regulation of lacrimal gland secretory processes: relevance in dry eye diseases. Prog Retin Eye Res 28:155–177

Dartt D, Willcox M (2013) Complexity of the tear film: importance in homeostasis and dysfunction during disease. Exp Eye Res 117:1

Doane MG (1981) Blinking and the mechanics of the lacrimal drainage system. Ophthalmology 88:844–51

Dursch TJ, Li W, Taraz B, Lin MC, Radke CJ (2018) Tear-film evaporation rate from simultaneous ocular-surface temperature and tear-breakup area. Optom Vis Sci 95(1):5–12

Gilbard JP, Farris RL, Santamaria J (1978) Osmolarity of tear microvolumes in keratoconjunctivitis sicca. Arch Ophthalmol 96(4):677–681

Gipson IK (2004) Distribution of mucins at the ocular surface. Exp Eye Res 78(3):379–388

Govindarajan B, Gipson IK (2010) Membrane-tethered mucins have multiple functions on the ocular surface. Exp Eye Res 90(6):655–663

Hamano H, Hori M, Mitsunaga S (1981) Measurement of evaporation rate of water from the precorneal tear film and contact lenses. Contacto 25(2):7–15

Himebaugh N, Nam J, Bradley A, Liu H, Thibos LN, Begley CG (2012) Scale and spatial distribution of aberrations associated with tear breakup. Optom Vis Sci 89(11):1590–1600

Holly FJ (1973) Formation and rupture of the tear film. Exp Eye Res 15(5):515–525

Jensen OE, Grotberg JB (1993) The spreading of heat or soluble surfactant along a thin liquid film. Phys Fluids A 75:58–68

Jossic L, Lefevre P, De Loubens C, Magnin A, Corre C (2009) The fluid mechanics of shear-thinning tear substitutes. J Non-Newton Fluid Mech 161(1–3):1–9

Kimball SH, King-Smith PE, Nichols JJ (2010) Evidence for the major contribution of evaporation to tear film thinning between blinks. Invest Ophthalmol Vis Sci 51(12):6294–6297

King-Smith PE, Fink B, Hill R, Koelling K, Tiffany J (2004) The thickness of the tear film. Curr Eye Res 29(4–5):357–368

King-Smith PE, Nichols JJ, Nichols KK, Fink BA, Braun RJ (2008) Contributions of evaporation and other mechanisms to tear film thinning and break-up. Optom Vis Sci 85(8):623–630

King-Smith PE, Fink BA, Nichols JJ, Nichols KK, Braun RJ, McFadden GB (2009) The contribution of lipid layer movement to tear film thinning and breakup. Invest Ophthalmol Vis Sci 50(6):2747–2756

King-Smith PE, Hinel EA, Nichols JJ (2010) Application of a novel interferometric method to investigate the relation between lipid layer thickness and tear film thinning. Invest Ophthalmol Vis Sci 51(5):2418–2423

King-Smith PE, Nichols JJ, Braun RJ, Nichols KK (2011) High resolution microscopy of the lipid layer of the tear film. Ocul Surf 9(4):197–211

King-Smith PE, Ramamoorthy P, Braun RJ, Nichols JJ (2013a) Tear film images and breakup analyzed using fluorescent quenching. Invest Ophthalmol Vis Sci 54:6003–6011

King-Smith PE, Reuter KS, Braun RJ, Nichols JJ, Nichols KK (2013b) Tear film breakup and structure studied by simultaneous video recording of fluorescence and tear film lipid layer images. Invest Ophthalmol Vis Sci 54(7):4900–4909

King-Smith PE, Kimball SH, Nichols JJ (2014) Tear film interferometry and corneal surface roughness. Invest Ophthalmol Vis Sci 55(4):2614–2618

King-Smith PE, Begley CG, Braun RJ (2018) Mechanisms, imaging and structure of tear film breakup. Ocul Surf 16:4–30

Lakowicz JR (2006) Principles of fluorescence spectroscopy, 3rd edn. Springer, New York

Lemp MA, Hamill JR (1973) Factors affecting tear film breakup in normal eyes. Arch Ophthalmol 89(2):103–105

Lemp MA, Bron AJ, Baudouin C, del Castillo JMB, Geffen D, Tauber J, Foulks GN, Pepose JS, Sullivan BD (2011) Tear osmolarity in the diagnosis and management of dry eye disease. Am J Ophthalmol 151(5):792–798

Lemp MA et al (2007) The definition and classification of dry eye disease: report of the definition and classification subcommittee of the international dry eye workshop. Ocul Surf 5:75–92

LeVeque RJ (2007) Finite difference methods for ordinary and partial differential equations: steady-state and time-dependent problems. SIAM, Philadelphia

Li L, Braun R, Maki K, Henshaw W, King-Smith PE (2014) Tear film dynamics with evaporation, wetting, and time-dependent flux boundary condition on an eye-shaped domain. Phys Fluids 26(5):052101

Li L, Braun RJ, Driscoll TA, Henshaw WD, Banks JW, King-Smith PE (2015) Computed tear film and osmolarity dynamics on an eye-shaped domain. Math Med Biol 33(2):123–157

Liu H, Begley CG, Chalmers R, Wilson G, Srinivas SP, Wilkinson JA (2006) Temporal progression and spatial repeatability of tear breakup. Optom Vis Sci 83:723–730

Liu H, Begley C, Chen M, Bradley A, Bonanno J, McNamara NA, Nelson JD, Simpson T (2009) A link between tear instability and hyperosmolarity in dry eye. Invest Ophthalmol Vis Sci 50:3671–79

Maki KL, Braun RJ, Driscoll TA, King-Smith PE (2008) An overset grid method for the study of reflex tearing. Math Med Biol 25(3):187–214

Mertzanis P, Abetz L, Rajagopalan K, Espindle D, Chalmers R, Snyder C, Caffery B, Edrington T, Simpson T, Nelson JD et al (2005) The relative burden of dry eye in patients' lives: comparisons to a us normative sample. Invest Ophthalmol Vis Sci 46(1):46–50

Miljanović B, Dana R, Sullivan DA, Schaumberg DA (2007) Impact of dry eye syndrome on vision-related quality of life. Am J Ophthalmol 143(3):409–415

Mishima S, Maurice D (1961) The oily layer of the tear film and evaporation. Exp Eye Res 1:39–45

Mota M, Carvalho P, Ramalho J, Leite E (1991) Spectrophotometric analysis of sodium fluorescein aqueous solutions. Determination of molar absorption coefficient. Int Ophthalmol 15(5):321–326

Nagyová B, Tiffany J (1999) Components responsible for the surface tension of human tears. Curr Eye Res 19(1):4–11

Nelson JD, Craig JP, Akpek EK, Azar DT, Belmonte C, Bron AJ, Clayton JA, Dogru M, Dua HS, Foulks GN et al (2017) TFOS DEWS II introduction. Ocul Surf 15(3):269–275

Nichols JJ, Mitchell GL, King-Smith PE (2005) Thinning rate of the precorneal and prelens tear films. Invest Ophthalmol Vis Sci 46(7):2353–2361

Nichols JJ, King-Smith PE, Hinel EA, Thangavelu M, Nichols KK (2012) The use of fluorescent quenching in studying the contribution of evaporation to tear thinning. Invest Ophthalmol Vis Sci 53(9):5426–5432

Nocedal J, Wright S (2006) Numerical optimization. Springer, Berlin

Nong K, Anderson DM (2010) Thin tilm evolution over a thin porous layer: modeling a tear film over a contact lens. SIAM J Appl Math 70:2771–2795

Norn M (1969) Desiccation of the precorneal film: I. Corneal wetting-time. Acta Ophthalmol 47(4):865–880

Norn MS (1970) Micropunctate fluorescein vital staining of the cornea. Acta Ophthalmol 48:108–118

Norn MS (1986) Tear film break-up time: a review. In: Holly FJ (ed) The preocular tear film in health, disease and contact lens wear. Dry Eye Institute Inc, Lubbock, pp 52–56

Olufsen MS, Ottesen JT (2013) A practical approach to parameter estimation applied to model predicting heart rate regulation. J Math Biol 67(1):39–68

Owens H, Phillips J (2001) Spreading of the tears after a blink: velocity and stabilization time in healthy eyes. Cornea 20(5):484–487

Păun LM, Qureshi MU, Colebank M, Hill NA, Olufsen MS, Haider MA, Husmeier D (2018) MCMC methods for inference in a mathematical model of pulmonary circulation. Stat Neerl 72(3):306–338

Peng CC, Cerretani C, Braun RJ, Radke CJ (2014a) Evaporation-driven instability of the precorneal tear film. Adv Colloid Interface Sci 206:250–264

Peng CC, Cerretani C, Li Y, Bowers S, Shahsavarani S, Lin M, Radke C (2014b) Flow evaporimeter to assess evaporative resistance of human tear-film lipid layer. Ind Eng Chem Res 53(47):18130–18139

Riquelme R, Lira I, Pérez-López C, Rayas JA, Rodríguez-Vera R (2007) Interferometric measurement of a diffusion coefficient: comparison of two methods and uncertainty analysis. J Phys D Appl Phys 40(9):2769

Sharma A (2003) Many paths to dewetting of thin films: anatomy and physiology of surface instability. Eur Phys J E 12(3):397–408

Sharma A, Ruckenstein E (1985) Mechanism of tear film rupture and formation of dry spots on cornea. J Colloid Interface Sci 106:12–27

Sharma A, Ruckenstein E (1986) An analytical nonlinear theory of thin film rupture and its application to wetting films. J Colloid Interface Sci 113:8–34

Siddique J, Braun R (2015) Tear film dynamics with evaporation, osmolarity and surfactant transport. Appl Math Model 39(1):255–269

Stapf MR, Braun RJ, King-Smith PE (2017) Duplex tear film evaporation analysis. Bull Math Biol 79(12):2814–2846

Stone HA (1990) A simple derivation of the time-dependent convective-diffusion equation for surfactant transport along a deforming interface. Phys Fluids A 2(1):111–112

Sullivan BD, Whitmer D, Nichols KK, Tomlinson A, Foulks GN, Geerling G, Pepose JS, Kosheleff V, Porreco A, Lemp MA (2010) An objective approach to dry eye disease severity. Invest Ophthalmol Vis Sci 51(12):6125–6130

Tietz NW (1995) Clinical guide to laboratory tests. W. B. Saunders, Waltham

Tiffany JM (1991) The viscosity of human tears. Int Ophthalmol 15(6):371–376

Tomlinson A, Khanal S, Ramaesh K, Diaper C, McFadyen A (2006) Tear film osmolarity: determination of a referent for dry eye diagnosis. Invest Ophthalmol Vis Sci 47(10):4309–4315

Tomlinson A, Doane M, McFayden A (2009) Inputs and outputs of the lacrimal system: review of production and evaporative loss. Ocul Surf 7:17–29

Trefethen LN (2000) Spectral methods in MATLAB. SIAM, Philadelphia

Varikooty J, Simpson TL (2009) The interblink interval i: the relationship between sensation intensity and tear film disruption. Invest Ophthalmol Vis Sci 50:1087–1092

Versura P, Profazio V, Campos E (2010) Performance of tear osmolarity compared to previous diagnostic tests for dry eye diseases. Curr Eye Res 35(7):553–564

Wang J, Fonn D, Simpson TL, Jones L (2003) Precorneal and pre-and postlens tear film thickness measured indirectly with optical coherence tomography. Invest Ophthalmol Vis Sci 44(6):2524–2528

Webber WRS, Jones DP (1986) Continuous fluorophotometric method measuring tear turnover rate in humans and analysis of factors affecting accuracy. Med Biol Eng Comput 24:386–392

Willcox MDP, Argüeso P, Georgiev GA, Holopainen JM, Laurie GW, Millar TJ, Papas EB, Rolland JP, Schmidt TA, Stahl U, Suarez T, Subbaraman LN, Ucakhan OO, Jones LW (2017) The TFOS DEWS II tear film report. Ocul Surf 15:369–406

Winter KN, Anderson DM, Braun RJ (2010) A model for wetting and evaporation of a post-blink precorneal tear film. Math Med Biol 27:211–225

Wolffsohn JS, Arita R, Chalmers R, Djalilian A, Dogru M, Dumbleton K, Gupta PK, Karpecki P, Lazreg S, Pult H, Sullivan BD, Tomlinson A, Tong L, Villani E, Yoon KC, Jones L, Craig J (2017) The TFOS DEWS II diagnostic methodology report. Ocul Surf 15:544–579

Wong H, Fatt I, Radke C (1996) Deposition and thinning of the human tear film. J Colloid Interf Sci 184(1):44–51

Wong S, Murphy PJ, Jones L (2018) Tear evaporation rates: what does the literature tell us? Cont Lens Anterior Eye 41(3):297–306

Wu Z, Begley CG, Port N, Bradley A, Braun R, King-Smith E (2015) The effects of increasing ocular surface stimulation on blinking and tear secretion. Invest Ophthalmol Vis Sci 56(8):4211–4220

Yeh PT, Casey R, Glasgow BJ (2013) A novel fluorescent lipid probe for dry eye: Retrieval by tear lipocalin in humans. Invest Ophthalmol Vis Sci 54(2):1398–1410

Yokoi N, Georgiev GA (2013) Tear-film-oriented diagnosis and therapy for dry eye. In: Yokoi N (ed) Dry eye syndrome: basic and clinical perspectives. Future Medicine, London, pp 96–108

Yokoi N, Georgiev GA (2019) Tear-film-oriented diagnosis for dry eye. Jpn J Ophthalmol 63:127–136

Zhang L, Matar OK, Craster RV (2003) Analysis of tear film rupture: effect of non-Newtonian rheology. J Colloid Interface Sci 262:130–48

Zhang L, Matar OK, Craster RV (2004) Rupture analysis of the corneal mucus layer of the tear film. Mol Simul 30:167–72

Zhong L, Ketelaar CF, Braun RJ, Begley CG, King-Smith PE (2018) Mathematical modelling of glob-driven tear film breakup. Math Med Biol 36(1):55–91

Zhong L, Braun RJ, Begley CG, King-Smith PE (2019) Dynamics of fluorescent imaging for rapid tear thinning. Bull Math Biol 81(1):39–80